University of Alberta

Prediction of the Active Layer Nanomorphology in Polymer Solar Cells Using Molecular Dynamics Simulation

by

Ali Reza Ashrafi Khajeh

A thesis submitted to the Faculty of Graduate Studies and Research
in partial fulfillment of the requirements for the degree of

Master of Science
in
Chemical Engineering

Department of Chemical and Materials Engineering

Fall 2012
Edmonton, Alberta

Abstract

The most important factor that determines the efficiency of bulk heterojunction polymer solar cells (PSC) is the active layer structure. Continuous domains of acceptor and donor material with thicknesses in the order of 10–30 nm must be formed to yield the highest efficiency in solar cells. Diblock copolymers are promising candidates for active layer material due to their tendency to self-segregate into such domains. Structure of diblock copolymers depends on three factors: Flory-Huggins interaction parameter (χ), total degree of polymerization (N) and volume fraction of the blocks (φ_i) in the block copolymer. The total degree of polymerization and volume fraction of blocks can be easily controlled while synthesizing the copolymer and hence χ parameter is the key to predicting the nanomorphology of diblock copolymers.

In the current thesis, a molecular dynamics (MD) simulation method is reported to calculate χ parameter for two different copolymers at different temperatures. χ parameter depicts a linear correlation with the reciprocal temperature which is consistent with the results reported in the literature. Moreover, the predicted nanomorphology for these systems is in good agreement with AFM results reported in the literature.

Acknowledgement

I would like to thank Prof. Phillip Choi for his continuous guidance and support without which this work was not possible. Moreover, I am grateful to Dr. Karthik Shankar for his contribution in my research.

This work is funded by National Science and Engineering Research Council of Canada.

All molecular dynamics simulation were performed using Materials Studio software package (MS Modeling version 4.0, Accelrys).

Table of Contents

List of Tables

List of Figures

Chapter 1

Introduction to Polymer Solar Cells

Environmental issues related to energy production from fossil fuels[1] and soaring crude oil prices in the last years have been the main stimulants for the development of renewable energy resources. More energy from sunlight strikes Earth in 1 hour than all of the energy consumed by humans in an entire year [2] and finding a cost-efficient way to capture it can solve the energy concerns of the human race for the foreseeable future. Silicon-based solar cell technology is the outcome of the intensive research endeavors in the last few decades but the production process of these panels is very energy intensive. Heavy weight, rigid physical form and high price are other main drawbacks of silicon-based solar cells.

Advent of organic semiconductors in the early 80s made it possible to fabricate solar PVs from polymeric materials. Some of the advantages of these so-called plastic solar cells include light weight, ease of processing, mechanical flexibility and versatility of the chemical structure.[3] The biggest advantage is the low cost of electricity generation, at 20% of the cost of traditional photovoltaics, which puts them on par with fossil fuels.[4]

The major differences between inorganic and organic solar cells can be summarized as follows:[5]

1) Inorganic semiconductors exhibit a band structure but organic semiconductors have discrete energy levels.
2) Exciton in an inorganic semiconductor disassociates immediately after it is produced but in organic semiconductors, the exciton binding energy is high and disassociation must be prompted.
3) Charge carrier mobilities in inorganic semiconductors are much higher than organics.
4) Optical absorption coefficient in organic materials is much higher than inorganics.

Research on polymeric solar cells started in early 90s and a few companies have been founded to produce PSCs on an industrial scale in recent years.[6-8]

The heart of a polymeric PV consists of three main layers: active layer, cathode buffer layer (electron transport layer) and anode buffer layer (hole polaron transport layer). The electricity generation takes place in the active layer. This layer is composed of two polymeric materials: electron donor and electron acceptor. The incident photon on these materials excites one of the electrons in the highest occupied molecular orbital (HOMO) to the lowest unoccupied molecular orbital (LUMO) and creates a Frenkel exciton (electron – hole pair). Since the electron donor has a lower electron affinity than the acceptor, the electron created subsequent to exciton dissociation, moves towards the acceptor and retains a positive charge on the donor. Hence, the donor material has an overall positive charge and the acceptor material has an overall negative charge. Finally, disassociated negative (electron) and positive (hole) charges migrate to the corresponding electron or hole transport layer. These charge transport layers (CTLs) act as a bridge between the active layer and electrodes and increase the device efficiency by reducing the resistance between active layer and electrodes.

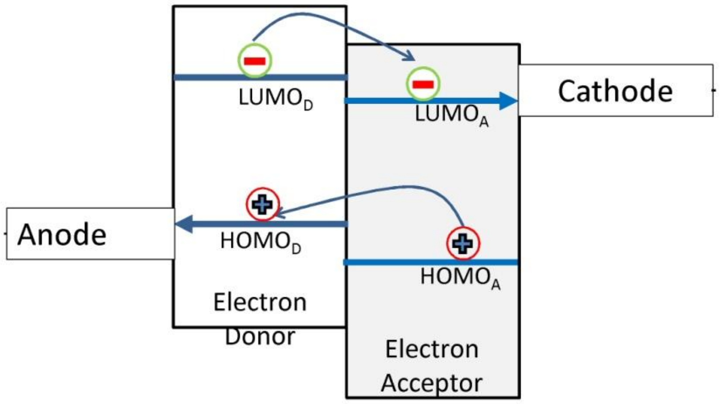

Figure 1.1 Energy level and charge disassociation in PSC

The outer surfaces of the device are electrodes which connect the device to the electrical circuit. We need one of these electrodes to be transparent because we need incident sunlight to diffuse into the active layer which is located in the middle of the device. A scheme of a typical polymeric PV is shown in figure 1.2.

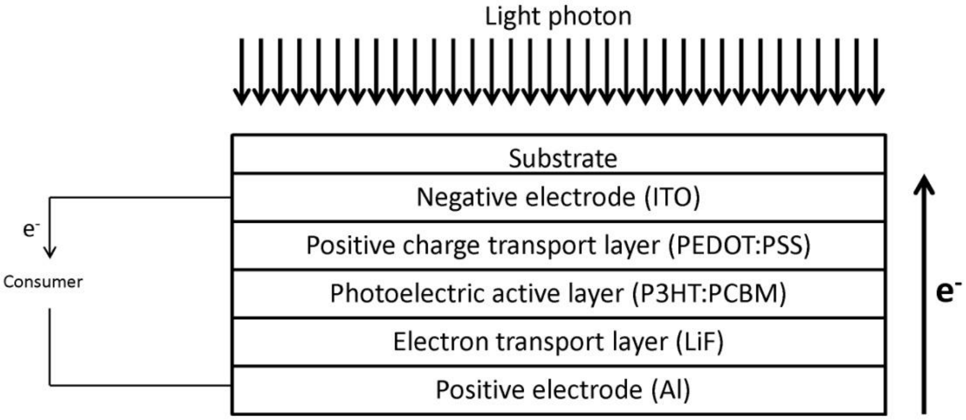

Figure 1.2: Schematic representation of a polymeric PV

1.1 Active Layer

1.1.1 Active Layer structure

In polymer solar cells (PSCs), the electricity generation takes place in the active layer. This layer is composed of two different types of molecules: electron donor (typically a *p*-type organic semiconductor) and electron acceptor (an *n*-type organic semiconductor). As a photon strikes the donor or acceptor, an electron is excited from highest occupied molecular orbital (HOMO) to the lowest unoccupied molecular orbital (LUMO) and a Frenkel exciton is created. Values of the exciton binding energy in organic semiconductors range from 0.1-1.5 eV, much higher than the thermal energy available to carriers at room temperature. The potential energy required to dissociate the exciton can be provided by an interface with suitable energy level matching. Typically, the formation of mobile charge carriers (electron and hole polarons) from a bound exciton at an interface requires an intermediate step involving the formation and dissociation of a charge transfer exciton.[9] Subsequently, the electron polaron is transferred towards the LUMO level of the acceptor material retaining a positive charge on the donor. The hole polaron which is created in the acceptor material will be transferred to the HOMO level of the donor retaining a negative charge on the acceptor material. However, for the exciton disassociation process to occur, the difference between the LUMO level of the donor material and LUMO level of the acceptor must be larger than the exciton binding energy. Moreover, the lifetime of excitons is limited and they ought to be dissociated before they recombine by radiative or non-radiative transitions. The exciton diffusion length (Λ), which is the average distance that excitons can migrate before decaying, is a function of electronic coupling, and energetic and structural disorder and given by $\Lambda = \sqrt{D\tau}$ where D is the diffusivity and τ is the exciton lifetime. In polymers where excitonic transport is dominated by Förster-mediated hopping, the singlet exciton diffusion length is given by[10]

$$\Lambda = \sqrt{\frac{\Phi_F}{6}\frac{R_0^3}{a^2}}$$

where Φ_F is the fluorescence quantum yield of the polymer, R_0 is the Förster radius and a is the average hopping distance. Λ being a function of the type of material, its purity and the type of packing, varies between different materials but is in the range of 5 – 20 nm for many conjugated polymers.[11] If the thickness of the donor and acceptor domains in the active layer is greater than this value, some fraction of excitons will recombine before disassociation and not contribute to the photocurrent.

The active layer structure in primitive PSC was planar heterojunction or bilayer heterojunction. In this structure, layers of the donor and acceptor material were built up on top of each other separately (Figure 1.3a). As mentioned earlier, excitons generated more than 5 – 20 nm away from the interface do not contribute significantly to the photocurrent. Layers thicker than this value will increase the resistance of the device and thus will decrease the overall efficiency so they are not favorable. Due to this reason, planar heterojunction active layers were built with a thickness in the order of the exciton diffusion length. However, a 20 nm thick film of a polymeric semiconductor is insufficient to optimally harvest sunlight. It is reported that to absorb greater than 95% of the incident light over the wavelength range of 450 – 600 nm, a P3HT film of 240 nm thickness is needed[12] so these devices tend to have a very low efficiency due to a very thin active layer. This fundamental trade-off between light absorption and exciton dissociation is known as the *exciton diffusion bottleneck*.

The second type of the active layer structure was a diffused bilayer structure in which donor and acceptor materials were diffused into each other in the contact region (Figure 1.3b). In this case the contact area between donor and acceptor materials is increased and charge movement path to reach the interface is shorter in comparison to the bilayer structure. The active layer thickness is still low due to the high resistance which limits the device performance. Chen et al.[13] fabricated a cell with PCBM as acceptor and MDMO-PPV as donor with a diffused bilayer structure in the active layer and gained an efficiency of 0.5% which was considered a high value in comparison to planar heterojunction solar cells.

The third type of structure is the bulk heterojunction (BHJ). The efficiencies of polymer photovoltaics experienced a major increase with the introduction of the BHJ structure. In this case, the donor and acceptor materials are completely mixed together and extremely short charge transport paths are attainable while having a thick active layer (Figure 1.3c). However, in the BHJ active layer, materials must form ordered and continuous phases to yield a high efficiency. In a discontinuous structure a significant fraction of charge carriers are trapped at dead-ends and will not reach the electrodes to contribute to the overall electricity generation. A disordered structure tends to have a low efficiency due to a high series resistance [14] and a low collection efficiency. In the BHJ structure, the donor and acceptor material should form phases with widths comparable to the diffusion length of excitons.

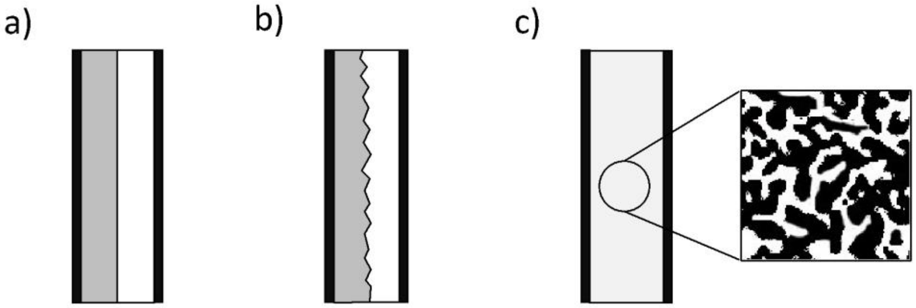

Figure 1.3: Schematic representation of a) Bilayer heterojunction, b) Diffused (stratified) bilayer and c) Bulk heterojunction.

As mentioned before, the thickness of the active layer in planar heterojunction was in the order of exciton diffusion length but it is approximately 200 nm for bulk heterojunction. The resulted increase in the thickness of the active layer can contribute to the increase in the high FF because the layer is free from pinholes and microcracks.[3]

Several methods have been proposed to improve the morphology of the active layer. In the following part, a brief description of these methods is presented

1.1.2 Active Layer Materials

As mentioned before, active layer is the main part of a polymer solar cell and performance of the device depends on the materials and morphology of this layer. In order to have a solar cell with high efficiency, materials used in the active layer must meet the following requirements:

- Absorption in the red and near-infrared portions of the AM 1.5 solar spectrum must be high since the maximum of the solar photon flux density occurs close to 700 nm.
- The difference between the HOMO level of the donor and the LUMO level of the acceptor must be large since the open-circuit voltage of the device under ideal conditions is determined by this difference.
- Demixing to form 5–20 nm size domains to create separate charge carriers and deliver them to electrodes.
- Charge carrier mobilities must be high and balanced: if the mobility of one of the charge carriers is significantly larger than the other, a local charge accumulation will decrease the device efficiency.
- Facile transport pathways for both types of charge carriers to be collected by their respective electrodes.
- Processibility from solution: This is an important factor in the realization of the suitable mass-production processes for device fabrication.
- High chemical purity and regioregularity (for polymers): The efficiency of the devices largely depends on the chemical purity of the used materials in

the active layer so they should be readily available in high purities and regioregularities (to minimize structural and compositional defects) .

- Stable morphology at high-temperatures that are part of the industrial production process: The processing of the subsequent layers; the hole transport layer (HTL) which typically is in the form of poly(3,4-ethylenedioxythiophene):poly(styrenesulfonate) (PEDOT:PSS) and the printable metallic back electrode requires drying at temperatures of 140 C for periods of time in the range of 5-10 min and unless the active layer presents a thermally stable nanomorphology it will not be compatible with such a process.[15]

In the following section a number of materials that has been used in polymer solar cells are introduced:

- **Acceptor Materials**:

1) C60

2) 1-(3-methoxycarbonyl)-propyl-1-phenyl-[6,6]-methanofullerene (PCBM)

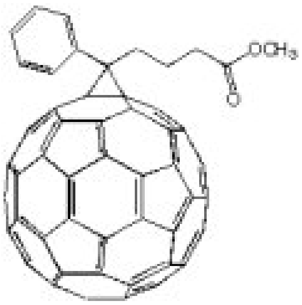

3) *N*,*N*′-ditridecylperylene-3,4,9,10-tetracarboxylic diimide (PTCDI-C13H27)

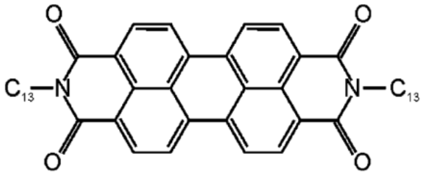

- **Donor materials:**

1) **Poly-3-hexylthiophene (P3HT):** P3HT is the acronym of poly(3-hexylthiophene), whose regioregular form is used in solar cells owing to its superior optoelectronic properties. P3HT has been used as the donor material in BHJ solar cells extensively in recent years. Self-organization of P3HT upon controlled evaporation improves the device efficiency by decreasing the device series resistance and increasing the short-circuit current. It has been reported that the series resistance of the 210 nm active layer with organized P3HT crystals is equal to that of a much thinner devices (48 nm thickness) with unorganized active layer.[16]

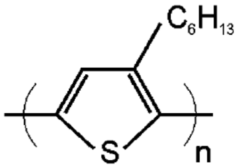

2) Chloroboronsubphthalocyanine (SubPc)

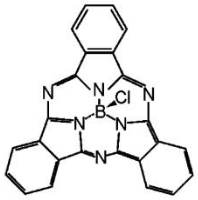

3) Chloroboronsubnaphthalocyanine (SubNc)

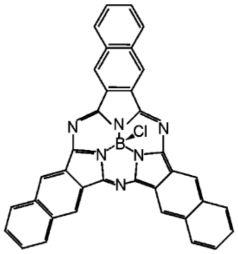

4) Copper phthalocyanine (CuPc)

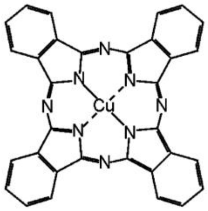

5) poly[2-methoxy-5-(3′,7′-dimethyloctyloxy)-1,4-phenylene vinylene] (MDMO-PPV)

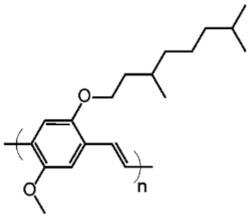

6) Poly[2,6-(4,4-bis-(2-ethylhexyl)-4H-cyclopenta[2,1-b;3,4-b_]-dithiophene)-alt-4,7-(2,1,3-benzothiadiazole)] PCPDTBT: which is based on a benzothiadiazole unit (acceptor) and a 4,4-bis(2- ethylhexyl)-4H-cyclopenta[2,1-b;3,4-b0]dithiophene unit (donor) that gives it an optical band gap around 1.46 eV.[16]

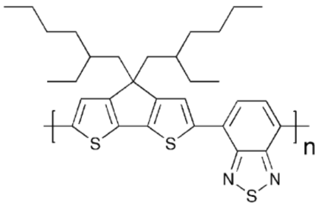

PCPDTBT

7) PCDTBT: PCDTBT is based on a 4,7-dithienylbenzothiadiazole unit and a soluble carbazole unit that gives it an optical band gap around 1.88 eV.[17]

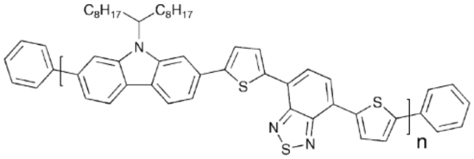

PCDTBT

1.1.3 Active layer morphology improvement methods

- Thermal treatment

Thermal annealing is a rather simple method to improve the nanomorphology of the active layer and hence overall efficiency of the device when the donor is P3HT. P3HT molecules have a tendency to organize and form crystals in their thermodynamic equilibrium state. However, during the fast growth of the active layer, the orientation of P3HT supermolecules is forced by the short timescale and is not thermodynamically stable. In the thermal annealing method, the produced layer is annealed at a higher temperature for a specific period of time. The enhanced molecular mobility due to a higher temperature enables the molecules of P3HT to diffuse through the blend and form aggregates. These aggregates improve the nanomorphology of the layer from disordered to a rather ordered structure which increases the device efficiency.

For instance, after annealing for 10 minutes in 110 C, the short-circuit current increased from 9.9 mA cm^{-2} to 10.6 mA cm^{-2} while the open-circuit voltage remained constant. The *fill factor*[1] increased from 60.3 to 67.7% and PCE improved from 3.5% to 4.4% under the standard AM1.5G 1 Sun test condition.[3] Power conversion efficiencies up to 5% have been demonstrated through the optimization of annealing temperature and time, achieved by annealing at 150 °C for 30 min.[18]

The size of the P3HT phase varies from 10 to 100 nm on annealing for 5 min at 100 ˚C.[19] Annealing at higher temperature or for longer periods of times will increase the size of these domains. Since the diffusion length of exciton is in the order of 5 – 20 nm, this will cause in lower device efficiency due to the charge carrier decay before they reach to acceptor/donor interface. The shape of the polymer crystals in the active layer can be tuned using different thermal annealing procedures and different solvents.[20]

Microwave irradiation has been suggested as an alternative method of heating but this method has not shown any superior results over conventional heating methods.

Thermal annealing on completed devices shows better device performance than cases when annealing is performed after active layer deposition and before top electrode deposition. This result indicates that thermal annealing changes the properties of the interface between active layer and top electrode.[18]

- Solvent annealing:

The morphology of the active layer blend can be promoted by controlling the vaporization rate of the solvent. This method is called “solvent annealing” or “solvent vapour annealing”. As mentioned before, P3HT supermolecules do not

---

[1] Fill Factor is the ratio of maximum obtainable power to the product of the open-circuit voltage and short-circuit current: $P_{max}/(V_{oc} \times I_{sc})$

have enough time to aggregate upon fast solvent vaporization so controlled removal of solvent can help P3HT molecules to self-organize.

It has been indicated that a thermal annealing treatment on completed device in addition to solvent annealing can improve PCE of the device.

Different methods of nanomorphology treatments in spite of huge differences in their procedure lead to the same PCE outcome of 4-5%. It has been demonstrated that these techniques lead to a common arrangement of components which consists of a vertically and laterally phase-separated blend of crystalline P3HT and PCBM. For the maximum device efficiency, the concentration of the donor materials must be greater near the device anode and the concentration of the acceptor material must increase towards the device cathode because this concentration profile increases the electrode selectivity.

- Additives:

Thermal and vapour annealing is effective only in the case of P3HT:PCBM pair due to the tendency of the polymer to self-organize. Nanomorphology of the acceptor-donor blends in BHJ active layers can be modified successfully by incorporation of suitable liquid or solid additives as well. The efficiency of PSC made of PCPDTBT and PC70BM increased from 2.8% to 5.5% by simply incorporating 17.5–25 mg/ml of 1,8-octanedithiol without any further annealing.[16]

In some cases solid additives can be helpful to attain the most effective morphology by acting as a nucleation agent for the donor polymer. For instance, the photovoltaic device power conversion efficiency prior to thermal annealing was enhanced by a factor of 2 by adding 5% of DHPT[3] (a copolymer including thieno-thiophene units) into the blend.[21]

- Vertically aligned nanostructures:

The ideal morphology to balance exciton dissociation and charge transport requirements is a columnar segregated structure, perpendicular to the device electrodes, in which the size of each donor or acceptor section is within an exciton diffusion length.[22] Different attempts has been made to attain this ideal structure but the devices fabricated using this approach has shown poor efficiencies so far.

1.2 Buffer layers

Buffer layers, interfacial layers or interlayers are used in PSC devices to improve the charge collection process.

Buffer layers are usually chosen based on their energy levels to improve charge collection on electrodes. However they can act as ‘‘protection’’ against the roughness of the substrate or the diffusion of the top electrode through the active layer, and can even act as oxygen and water scavengers. Moreover, in some cases they can enable better light absorption, leading to enhanced efficiencies, thus having the additional role of ‘‘optical spacer’’. The usual structures include both anode buffer layer (ABL) and cathode buffer layer (CBL).

1.2.1 Anode Buffer Layer

The role of an anode buffer layer (ABL) is to increase the efficiency of collection of positive charge carriers. Open-circuit voltage is governed by the energy levels of the donor and acceptor materials in case of ohmic contacts. ITO is usually used in solar cells as the electrode due to its transparency. However, the non-ohmic character of the ITO/donor or ITO/acceptor interface affects the maximum attainable V_{oc} in conventional and inverted solar cells. ITO in principle is able to collect both positive and negative carriers because of the position of its work function with respect to the typical energy levels of the active layer materials, and it cannot provide the required selectivity.

The main requirements for an anode buffer layer are:[5]

1. It ought to provide an ohmic contact with the donor material;
2. It ought to transport positive carriers efficiently (hole polaron transporting);
3. It ought to block negative charge carriers (electron blocking).

In addition, the ideal anode buffer layer should be stable and should not increase the device series resistance (R_s). Finally, transparency is required in the conventional device configuration.

In order to increase ITO layer selectivity for hole polarons, (when used as anode buffer layer) ABL consisting of a poly(3,4-ethylenedioxithiophene)(PEDOT) doped with poly(styrene sulfonicacid) (PSS), was used. PEDOT is not soluble in water but chemical polymerization in the presence of PSS aqueous polyelectrode yields a colloidal PEDOT:PSS dispersion suitable for aqueous processing.[23]

The high work function of PEDOT:PSS (usually reported between 4.8 and 5.2 eV)[24] allows the formation of an ohmic contact with most common donor polymers. There are different types of PEDOT:PSS commercially available in the market and their performances are slightly different. The thickness of ABL affects only the short-circuit current of the device. J_{sc} slightly decreases with the increasing thickness. Generally the thickness of this layer is 60–165 nm.[5] The acidity of PEDOT:PSS dispersion can cause ITO corrosion[25] and its work function is largely affected by its water content.[26] In terms of the electron blocking, PEDOT:PSS is not the best choice and other materials with better negative charge blocking are available.[5]

1.2.2 Cathode Buffer layer

As was the case for the anode buffer layer, cathode buffer layer material should have several special characteristics. It has to provide an ohmic contact with the acceptor material and it has to transport negative charge carriers and block positive charge carriers.

Several materials have been tried as cathode buffer layer by different groups. Brabec et al.[27] used lithium fluoride as the cathode buffer layer to improve the device efficiency with the Al as electrode. They explained that deposition of a thin LiF layer under Al electrode would result in an increase of the fill factor and open-circuit voltage as well as decrease the series resistance. As a result, the device efficiency increased by over 20% to η=3.3%.

Jiang et al.[28] demonstrated that CsF buffer layer can improve device performance. They used CsF along with Al as cathode for a solar cell with MEH-PPV:PCBM as the active layer and demonstrated that the efficiency, open-circuit voltage and resistance are improved by the deposition of 0.4 – 3.0 nm CsF interlayer.

Chen et al. suggested cesium carbonate as cathode buffer layer[29]. They demonstrated that the maximum open-circuit voltage of the device with Cs_2CO_3 interlayer is close to the difference between HOMO level of the donor and LUMO level of the acceptor implying the contact between active layer and electrode is ohmic when cesium carbonate is used as the buffer layer. The device efficiency increased from 2.3% to 3.1% as a result.

Kim et al.[30] used titanium sub-oxide (TiO_x) as the cathode buffer layer. The TiO_x layer can be deposited using solution-based methods which makes it suitable for industrial production. The efficiency of the device increased from 2.3% to 5% by using TiO_x as the cathode buffer layer under Al electrode. TiO_x can be used in both conventional and inverted solar cell because it is transparent and does not need high temperature in the deposition process.

ZnO is another metal oxide used as cathode buffer layer. Zinc oxide has been mainly investigated as a cathode buffer layer in inverted polymer solar cells because the high temperature processing required to achieve its crystallinity is not suitable for the conventional device structure. White et al.[31] used ZnO in their device with P3HT:PCBM as active layer and obtained a power conversion efficiency of 2.58% in their inverted solar cell.

1.3 Different PSC structures

1.3.1 Conventional Structure

The conventional device structure is shown in the Figure 1.4. In this structure, the ITO electrode is used as the anode to collect positive charge carriers (hole polarons). PEDOT:PSS is deposited as the anode buffer layer followed by the active layer. Electron-selective layer (LiF, ZnO or TiO_2) is deposited on the active BHJ layer to improve the electron collection efficiency in the cathode and also prevent the diffusion of the top metal electrode into the active layer. Finally, a low work-function metal electrode (Al or Ca/Al) is evaporated as cathode.

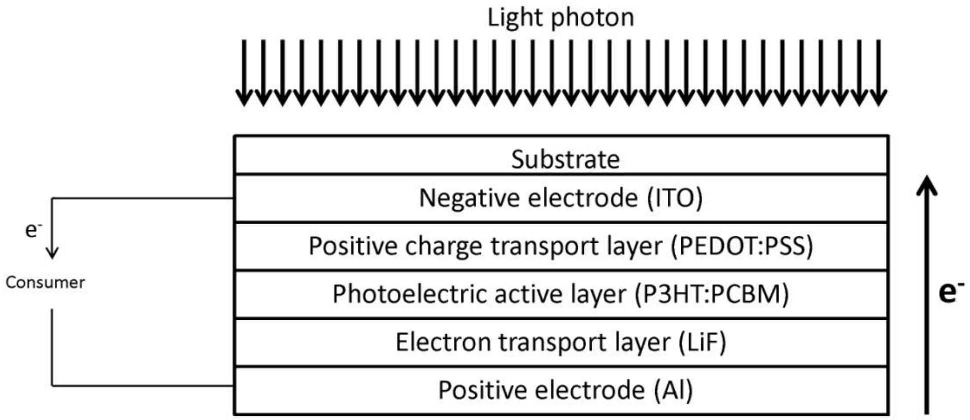

Figure 1.4: Conventional device structure

There are two main drawbacks associated with this device structure when it comes to realization of a suitable industrial fabrication process:

1) The ITO electrode maybe etched over time due to the exposure to the acidic PEDOT:PSS layer. [32]
2) The vacuum deposition of the low function metallic electrode increases the fabrication costs. Moreover, exposure to the ambient air can lead to the oxidation of electrode and decrease in efficiency.

1.3.2 Inverted structure

To overcome the two abovementioned difficulties in the fabrication of the conventional solar cells, the inverted solar structure has been proposed. In this type of solar cells the direction of flow of electrons is the opposite of conventional solar cells meaning that the transparent electrode (e.g. ITO) is the anode of the device.

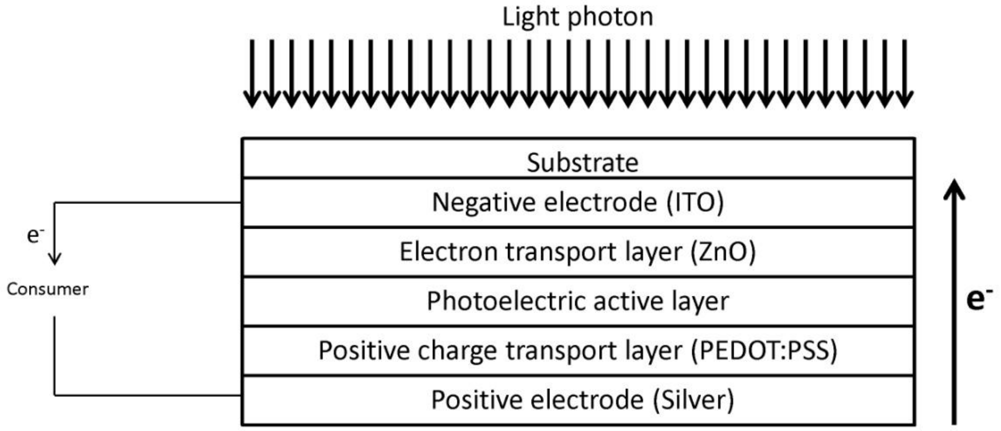

Figure 1.5: Inverted device structure

For efficient charge collection, work functions of anode and cathode should be matched to the highest occupied molecular orbits (HOMO) of donor and the lowest unoccupied molecular orbits (LUMO) of acceptor, respectively.[33] In conventional solar cells, low work function metal acts as the top cathode electrode while in the inverted structure, the low work function modified ITO which is the lower electrode acts as the cathode and a high work function metal acts as top anode. Since the probability of contamination of a low work function metal is high when acts as the top electrode due to the exposure to air and oxidation, its use as the bottom layer will decrease this possibility and increase the device lifespan. Moreover, the inverted configuration allows the use of higher work function and less air-sensitive electrodes (e.g. Au, Ag and Cu) as the top electrode for hole polaron collection.[32] Use of the high work function top electrode is not problematic since its potential oxidation will increase its work function from 4.3 to 5 ev and thus benefit the device efficiency.[31]

In addition, inherent vertical phase separation in the polymer active layers[33] matches the device configuration better in the inverted case.

The other advantage of inverted solar cell is that there is no need for the PEDOT:PSS buffer layer (Although it could be used). It was noted that the acidic PSS has an adverse effect on the metallic electrode.[33]

1.3.3 Tandem solar cells

It has been mentioned that the absorbance spectrum and thus device efficiency is largely limited by the bandgap of the active layer materials. Inorganic materials have a band structure and they can absorb all photons in sunlight that have more than a certain energy ($\lambda < 1.12$ microns in the case of silicon wafer) but in the case of organic semiconductors, they have discrete energy levels and only absorb certain wavelengths from solar radiation. The excitonic absorption of organic semiconductors is characterized by the presence of peaks and valleys as opposed to a single band-edge as with inorganic semiconductors. Having one pair of acceptor/donor materials, we will be able to absorb photons in certain spectral regions of the incident sunlight. The idea behind tandem solar cells is to use two (or more) pairs of acceptor/donor materials in the active layer to absorb a greater portion of the incident light.

Generally tandem solar cells are divided into three categories based on the material in their active layer:

A) In the first category, active layer in both the bottom and top cells are made from low molecular weight polymers using vacuum-deposition technology:

The advantage of using low molecular weight molecules in tandem cells is that vacuum-depositing can be used to fabricate the cells without affecting previous layers while in the case of solution-processed materials there is a probability that previously deposited layers be partially or fully dissolved in the top layers. The disadvantages of vacuum depositing are lower production rate and higher costs. Hiramoto et al.[34] fabricated one example of this type. They used the same materials for active layer in both cells with an ultra-thin Au layer between them. Using this structure, the photovoltage almost doubled while the photocurrent density depended in the thickness of the Au interlayer.

Tandem solar cells can include more than two layers. Yakimov et al.[35] fabricated their solar cells including 2, 3 and 5 layers. The efficiency of those devices was dependent on the intensity of the incident light. Tandem solar cells with two layers were the most efficient in terms of the device PCE at 1 sun illumination (100 mW cm^{-2}).

Yakimov et al.[35] used a discontinuous layer of Ag as charge recombination sites as shown in figure 1.6. All sub-cells were a single heterojunction of PTCBI/CuPc as Acceptor/donor respectively. The thicker Ag interlayer resulted in the same voltage but lower photocurrent which can be attributed to the lower transparency of thicker layer which allows a lower solar radiation in the second cell.

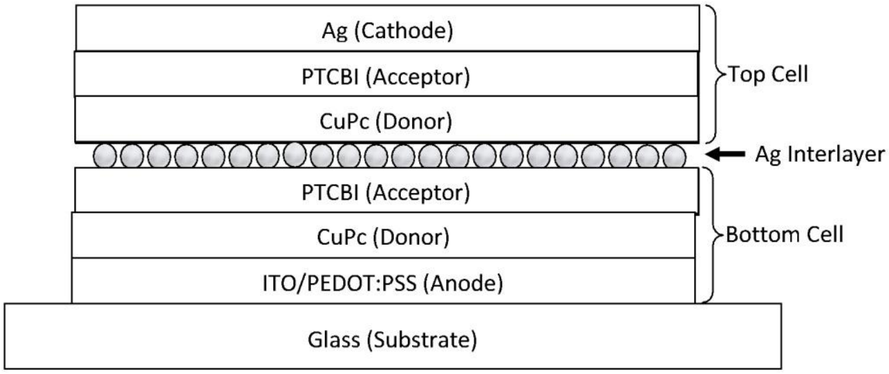

Figure 1.6: Schematic representation of the device by Yakimov et al.[35]

Uchida et al.[36] used a rather complex charge recombination layer in their device. The charge recombination zone in their tandem cell consisted of a 5 Å thick Ag nanocluster layer and a 50 Å thick 4,48,49-tris(3-methyl-phenyl-phenyl-amino) triphenylamine (m-MTDATA) doped with 5 mol % tetrafluoro-tetracyano-quinodimethane (F_4-TCNQ). The same group later got the efficiency of η=(5.7±0.3) % using this new inter-layer.[37]

Theoretically, when several cells are connected in series, the total voltage of the device must be sum of the single cells under ideal circumstances while current will be less than the current of single cells so it is important to optimize the thickness and order of single cells so that photocurrents from single cells are all equal.

4-3 B) Hybrid tandem organic solar cells in which the bottom cell is processed from polymers by solution processing while low molecular weight polymers are used in the top cells:

In order to improve the efficiency of a P3HT:PCBM based solar cell, Dennler et al.[38] vacuum deposited another cell composed of small molecules zinc phthalocyanine (ZnPc) as donor and C_{60} as acceptor on top of the first layer. This specific type of tandem cell in which one of the sub-cells is composed of heavy polymer molecules while the other is from small molecules is called Hybrid tandem organic cell. A layer of clusters of 1 nm gold (Au) was used as intermediate layer between the two sub cells, which served as a recombination center.

Results obtained from the tandem cell are compared with the reference single cells in the table 1. The photovoltage of the tandem cell is equal to the sum of single cells that proves the Au inter-layer was successful. The disadvantage of this device lies in the fact that photocurrent is limited to the lower value of sub-cells and this makes the optimization of the thicknesses of layers necessary which has not been done in the experiment by Dennler et al.[38]

Cell	J_{sc} (A/m^2)	V_{oc} (V)	FF (%)	PCE (%)
Tandem	48	1.02	45	2.3
Ref. Bottom	85	0.55	55	2.6
Ref. Top	93	0.47	50	2.2

Table 1.1: performance of the tandem and reference cells fabricated by Dennlar et al.[38]

The other disadvantage of this device structure is the high fabrication cost because the top layer which is composed of small molecules must be deposited in very high vacuum (10^{-6} mbar).

4-3 C) Fully solution processed tandem cells in which both bottom and top cells are made from heavy polymeric molecules/fullerene derivatives using solution processing:

The problem in the fabrication of these cells is that deposition of the top layer using spin-coating may damage the bottom layer especially when the same solvents are used for both layers. Hence, the interlayer must be thick enough to prevent solvent leak to the bottom layer and must be transparent at the same time which makes finding a suitable material difficult.

One of the ways to overcome the abovementioned problem in the fabrication of fully solution-processed tandem cells is to process them on separate substrates. Shrotriya et al.[39] fabricated two identical bulk heterojunction single cells onto different glass substrates and positioned them on top of each other and then connected them in series and parallel to study the variance in photocurrent and photovoltage in comparison with the single cells. To let the unabsorbed portion of light to diffuse into the top cell, the cathode in the bottom device was made from semitransparent lithium fluoride (LiF)/aluminum (Al)/gold (Au). Maximum transparency of 80% was achieved in the semitransparent electrode. Upon stacking, in series configuration the open-circuit voltage and in the parallel configuration the short-circuit current almost doubled.

- **Separating materials in tandem solar cells:**

Kawano et al.[40] used ITO layer in their work as the transparent interlayer. The most important aspect of their work was the method they used to deposit ITO interlayer. They deposited ITO by dc magnetron sputtering in 1 Pa of argon gas without substrate heating. The presence of argon gas into the deposition chamber prevented damaging of the active layer of the bottom cell during deposition of the ITO layer.

Another example of interlayer is solution-processible ZnO layer. Gilot et al.[41] deposited the recombination layer between the active layers by spin coating ZnO nanoparticles from acetone, followed by spin coating neutral *p*H poly(3,4-ethylene-dioxy-thiophene) from water and short UV illumination of the completed device. Conventional PEDOT:PSS layer may not be used as it could dissolve ZnO layer. The key advantage of this procedure is that each step does not affect the integrity of previously deposited layers. The open-circuit voltage (V_{oc}) for double and triple junction solar cells is close to the sum of the V_{oc}'s of individual cells.

This type of interlayer has two desirable properties. The very high transparency of the ZnO/PEDOT interlayer prevents the loss of solar radiation due to the opacity of the interlayer. The second favourable characteristic of this type of interlayer is the possibility to fabricate the whole multi-junction solar cell from solution which is important in large-scale production of polymer solar cells.

Interlayers in tandem solar cells can be fabricated from titanium oxide (TiO_x). [42] As in the case of ZnO, this type of interlayer has the same advantages of high transparency and solution processibilty.

1.4 Fabrication Methods

Most of the research activities have been focused on the efficiency increase of organic cells in laboratory while realization of suitable industrial methods to fabricate these cells is as important as lab-scale enhancements in the cell structure. Krebs[43] presented a comprehensive overview of the potential fabrication methods and a brief summary of the work is presented here.

Film forming techniques can be divided into two main categories: the first category consists of techniques suitable for individual processing of small substrates (i.e. spin coating, doctor blading and casting). The second category is methods developed for mass production of film materials in paper, plastic and textile industries. These methods are called roll-to-roll coating or reel-to-reel coating (abbreviated R2R coating).

1.4.1 Lab-scale methods

1) Casting: is a manufacturing process by which a liquid material is usually poured into a mold, which contains a hollow cavity of the desired shape, and then allowed to solidify. In this method no sophisticated equipment is needed but there is no control over the thickness of the film.

2) Spincoating: The typical spincoating operation involves application of a liquid to a substrate followed by acceleration of the substrate to a chosen rotational speed. Alternatively the liquid solution may be applied while the substrate is spinning. The angular velocity of the substrate (ω) with the overlying solution results in the ejection of most of the applied liquid

where only a thin film is left on the substrate. The method is the most used one because it is highly reproducible. The method is also used in the manufacturing process of digital versatile disks (DVD) and compact discs (CD). Sample thickness, morphology and surface topology are important factors which depend on rotational speed, viscosity, volatility, diffusivity, molecular weight and concentration of solutes. Thickness (d) of the obtained film can be obtained using: $d = k\omega^{\alpha}$ in which α is around 0.5 in many cases. This method is not suitable for mass production because firstly substrates should be handled individually, secondly patterning of films is not possible and thirdly this technique is not parsimonious in terms of ink consumption.

3) Doctor Blading: This technique works by placing a sharp blade at a fixed distance from the substrate surface (typically 10 – 500 μm) that is to be coated. This technique allows the deposition of the films to be reproducible and well-defined. The film thickness is about half of the gap distance.

   In terms of operational complexity and instrument cost, doctor blading and Spincoating are almost alike but the extensive use of Spincoating method in laboratories is due to two main reasons. Firstly, it takes some trial and error in doctor-blading method to find appropriate conditions to reach the desired film thickness so there is some material loss in this stage. Secondly, this method is relatively slow and if the material is prone to crystallize in high concentrations, this will most likely occur in doctor-blading method. However doctor-blading seems to be more suitable in industrial scale fabrication.

4) Screen printing: In this method a screen of woven material or steel mesh is used. To create the desired pattern on the substrate, the screen is impregnable to the solution in the areas that we do not want to be covered

and it is open to solution in the areas that we want them to be covered with the solution. To perform printing, the screen is placed on top of the substrate and the solution ink is distributed on it. Screen printing is considered as a favorable process to fabricate solar cells.

5) Ink jet printing: This method is similar to typical ink jet paper printers in which droplets of ink (solution in the case of solar cell fabrication) are created using mechanical nozzle or by heating the solution. These droplets are then electrostatically charged and accelerated towards the substrate by an electric field. For this method to work properly, the solvents must be non-volatile. Moreover, surface tension of the solution must be high to make the generation of droplets possible.

1.4.2 Roll-to-roll techniques for industrial purposes

The abovementioned techniques are suitable to fabricate a single device in the lab while in industry we need some steady-state processes to fabricate the cells. Krebs discussed some of the potential routes for this purpose in reference 39 including Knife-over-edge coating, meniscus coating, Slot die coating, Gravure coating, Curtain, multilayer slot and slide coating. Other film forming techniques that may become relevant are spray coating, flexographic printing, offset lithography, electrophotography, electrography and magnetography. These methods are discussed extensively in the abovementioned review paper. The only well-reported industrial fabrication method for solar cell fabrication is “ProcessOne”.[44] The following is the brief description of the fabrication of solar cell using this process:

Step 1: ITO electrode patterning

The most commonly employed transparent conductor is indium-tin-oxide (ITO), which is commercially available on flexible PET foil. In this case, a 130 mm

PET substrate is employed with a fully covering layer of ITO with a thickness of 90 nm, which had been sputtered using a vacuum roll-to-roll process. Due to the relatively high sheet resistivity of the ITO it is necessary to pattern the ITO, so that smaller cells can be connected in series.

This involves the screen printing in a Klemm printer line of an etch resist and UV curable ink onto the ITO-covered PET material, with the desired ITO pattern. This Klemm line comprises unwinder, flat bed screen printer, UV-curing oven and rewinder. The ITO is etched using $CuCl_2$(aq) followed by washing, stripping the etch resist and drying.

Step 2: Electron transport layer coating

Three processes comprise this step. First the ZnO ink which consists of ZnO nanoparticles is prepared. ZnO nanoparticles are synthesized by caustic hydrolysis of $Zn(OAc)_2$-$2H_2O$, heated and stabilized with methoxyethoxyacetic acid (MEA), and mixed with acetone, to give ZnO nanoparticles in acetone. This stock solution is diluted to give the final ink that is microfiltered through a 0.45mm Teflon filter immediately prior to coating. The concentration of ZnO nanoparticles in the final coating ink is 30 mg/ml.

In the slot-die coating it is necessary to clean the ITO substrate by passage through the system using corona treatment, web cleaning and washing using isopropanol followed by drying at 140ºC. The material is again dried at temperatures up to 140ºC. This procedure polymerizes the film containing the ZnO nanoparticles and gives insoluble films of zinc oxide.

Step 3: Active layer deposition

The ink for the active layer is prepared by dissolving commercially available P3HT (18–24 mg/ml) and PCBM (16–22 mg/ml) in chlorobenzene at 120 C for 3h. The ratio between P3HT and PCBM is typically 10:9. The blend is coated on the substrate with the ZnO layer using 2 mL per linear meter, resulting in 4.85 mm layer of wet thickness, which leads to a final dry layer thickness of 127 nm.

Step 4: PEDOT:PSS deposition

For the ink preparation PEDOT:PSS is diluted slowly with isopropanol using stirring until a solution viscosity of 270mPa.s was obtained. The wetting of P3HT:PCBM by PEDOT:PSS is not very good and because the use of corona treatment is not possible, it is useful to mix isopropanol into the PEDOT:PSS and also wet the active layer with isopropanol, immediately before the slot-die coating head. The devices are also prewashed with isopropanol during coating because this procedure results in much smoother films and better interfaces between the active layer and the PEDOT:PSS layer. The wet thickness of this layer is usually 75 µm and resulted in a dry layer thickness of 20 nm.

Step 5: Back electrode deposition

The screen printing of the silver back electrode is carried out on a flat bed roll-to-roll screen printer.

Step 6: Lamination

Complete lamination of the modules is carried out in several. Firstly, the adhesive is laminated onto the barrier foil. The barrier material with the lined adhesive could then be cut to a width of 250 mm for the backside in order to enable lamination of the active areas, while exposing some of the silver bus bars for electrical connections during roll-to-roll IV-testing. After application of the adhesive onto the barrier foil, it is laminated onto the unencapsulated solar cell material, on both sides of the devices.

1.5 Drawbacks of polymer solar cells

- Absorbance spectrum: As mentioned before, in spite of silicon-based photovoltaics that absorb all solar spectrum with energy more than a special value, polymer solar cells due to their discrete energy levels absorb only a certain wavelength range from solar radiation. This means that with a single acceptor/donor pair, we will not be able to convert all solar energy to electricity.

- Low efficiency: Although efficiencies higher than 8% (8.3% by Heliatech[45]) have been reported in the literature for polymer solar cells, these values are obtained in gloveboxes and under special conditions. The efficiency of industrially fabricated cells are around 1%[40] and is very low comparing to silicon technology which yields efficiencies of 18% for crystalline silicon technology and 25% for concentrator photovoltaics (CPV).[46]
- Lower lifetime: Polymer molecules are more susceptible to degradation by oxygen/water or under the effect of the UV portion of sunlight.[47] Inorganic materials have a lifetime in the order of 25 years[46] while the lifespan of a polymer solar cell is in the order of 1 year[44] which is considered as a big barrier in the industrialization of these cells

Chapter 2

Phase Separation in Block Copolymers

Before discussing about the thermodynamic theories of phase separation in block copolymers, it is beneficial to discuss briefly about the fundamental thermodynamic concepts in mixing of monomeric and polymeric liquids.

Gibbs free energy is usually used to characterize the favourability of any change from thermodynamic aspect. It is defined as:

$$G = U + PV - TS = H - TS \qquad 2.1$$

$$\Delta G_{mix} = \Delta H - T\Delta S \qquad 2.2$$

In which *U* is the internal energy, *P* is pressure, *V* is volume, *T* is temperature, *S* is entropy and *H* is enthalpy of the system.

Other properties associated with any process can be obtained from free energy of mixing expression:

$$\Delta H = \left(\frac{\partial \left(\frac{\Delta G}{T} \right)}{\partial \left(\frac{1}{T} \right)} \right)_{P,N_i} \qquad 2.3$$

$$\Delta S = -\left(\frac{\partial \Delta G}{\partial T} \right)_{P,N_i} \qquad 2.4$$

$$\Delta V = \left(\frac{\partial \Delta G}{\partial P}\right)_{T,N_i} \qquad 2.5$$

In which ΔH, ΔS and ΔV are enthalpy, entropy and volume change of the system, respectively.

2.1 Free Energy of Mixing

For the mixing process, free energy (ΔG_m) is defined as:

$$\Delta G_m = G_{mix} - \sum_{i=1}^{C} G_i \qquad 2.6$$

In which G_{mix} and G_i are Gibbs free energies of the mixture and pure components and C is the total number of the components. The basic condition for the favourability of the mixing or stability of the mixture is:

$$\Delta G_m < 0 \qquad 2.6$$

Moreover, a second condition must be satisfied as well. The rationale behind this condition is depicted in figure 2.1:

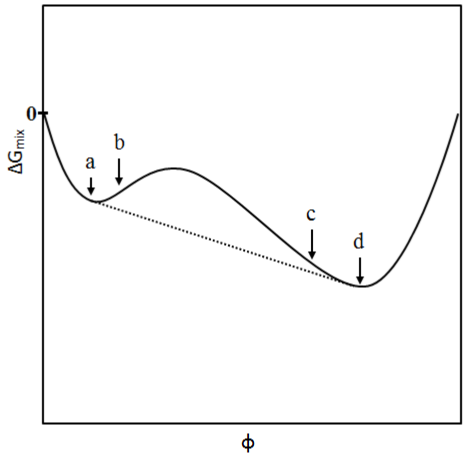

Figure 2.1: ΔG_{mix}–φ graph for a hypothetical system.

In the concentration range between points a and d, ΔG_{mix} is negative but the solution in this range will not be stable since it can reach lower free energy levels by separation into two phases. The boundaries of *global stability* can be found using the intercept of the common tangent line with the graph.

For a solution to be *locally stable*, the curvature of the ΔG–φ curve must be positive in addition to the above conditions:

$$\frac{\partial^2(\Delta G_{mix})}{\partial\varphi^2} \geq 0 \qquad 2.8$$

In Figure 2.1, the volume fraction range of $0 < \varphi < b$ and $c < \varphi < 1$ is *locally stable*.

2.2 Monomeric mixtures

2.2.1 The Ideal Solution

In the ideal solution, interactions between A and B species in the mixture are assumed to be equivalent to the interactions between the pure components.

$$\varepsilon_{AB} = \varepsilon_{AA} = \varepsilon_{BB} \qquad 2.9$$

Moreover, the size and shape of the A and B species must be the same. The only distinguishing features between species that form ideal solution are those irrelevant to mixing like color.

There are quite a few number of species in reality that can interact based on the ideal solution law but ideal solution is a good starting point to develop compatibility theories for real solutions.

The only contribution to the free energy change of mixing in ideal solutions is from combinatorial entropy.

$$\Delta G_{mix} = -T\Delta S_{com} \qquad 2.10$$

in which ΔS_{com} is the combinatorial entropy. As a result of the mixing process the total possible configurations of the system increases meaning that the mixing entropy is always positive. The combinatorial entropy for a system containing particles of the same shape and size is:

$$\Delta S_{com} = -kN_0 \sum_{i=1}^{C} x_i \ln x_i \qquad 2.11$$

in which x_i is the molar fraction of species i in the system.

For binary solutions with spherical components of the same shape and size:

$$\Delta S_{com} = -R(N_1 \ln x_1 + N_2 \ln x_2) \qquad 2.12$$

where N_i is the total number of i particles in the mixture.

2.2.2 Regular Solutions

The concept of regular solutions was introduced by Hildebrand in 1927.[48] In this treatment, the enthalpy term is included in the free energy of mixing. The *exchange energy, w,* is defined as:

$$w_{ij} = \varepsilon_{ij} - \frac{1}{2}(\varepsilon_{ii} + \varepsilon_{jj}) \qquad 2.13$$

In which ε_{ij} is the interaction energy between *i* and *j* pair and the total enthalpy of mixing can be calculated by sum of the all pairs' contributions:

$$\Delta H_{mix} = \sum_{i=1}^{C}\sum_{j>i}^{C} z w_{ij} n_i x_j \qquad 2.14$$

in which *z* is the coordination number, the number of components adjacent to the component *i*.

It is a good practice to convert the n_i to molar fraction of components (x_i) in the above equation:

$$\Delta H_{mix} = N_0 \sum_{i=1}^{C}\sum_{j>i}^{C} z w_{ij} x_i x_j \qquad 2.15$$

In which N_0 is the total number of components in the system.

The entropy contribution to the free energy of mixing in regular solutions is the same as the ideal solutions. This means that even if particles in the system interact with each other, either favorably or unfavorably, the total number of available configurations for the specific component will be the same as in the ideal solution in which there are no forces between the particles of the system. Therefore the free energy of mixing is:

$$\Delta G_{mix} = \Delta H_{mix} - T\Delta S_{mix} = \sum_{i=1}^{C}\sum_{j>i}^{C} N_0 z w_{ij} x_i x_j + kTN_0 \sum_{i=1}^{C} x_i \ln x_i \qquad 2.16$$

in which N_0 is the total number of particles in the system.

For binary systems, Gibbs free energy of mixing can be obtained by adding *Van Laar heat of mixing* term to the ideal entropy of mixing term*:*

$$\Delta G_{mix} = RT(N_1 \ln x_1 + N_2 \ln x_2) + A_{12}\varphi_1\varphi_2(V_1N_1 + V_2N_1) \qquad 2.17$$

A_{12} is the Van Laar parameter. Equation 2.17 is simplified form of equation 2.16 for binary solutions.

2. 3 Polymer mixtures

The above equation for regular mixtures is in good agreement with the monomeric experimental results but when it comes to the polymeric solutions, there is a big difference between vapor pressure predictions made using equation 2.16 and the experimental results. This disagreement prompted scientists to use lattice models to derive an expression for the combinatorial entropy of chain-like components. In these lattice models, all sites have the same volume which is usually taken equal to the solvent volume and polymer molecules occupy many lattice sites. In the lattice representation of polymer molecules, at least two adjacent sites must be occupied by the polymer to ensure polymer connectivity. If we have two polymers, A and B, assuming that the molar volume of the segments of A is smaller than B, the cell volume will be equal to v_A (segment molar volume of A). The total system volume, V, can be divided into N_t cells so that:

$$Nt = N_A + N_B = N_A + V_B/v_A$$

Where N_A is the number of segments in polymer A and N_B is the number of equivalent segments in polymer B.

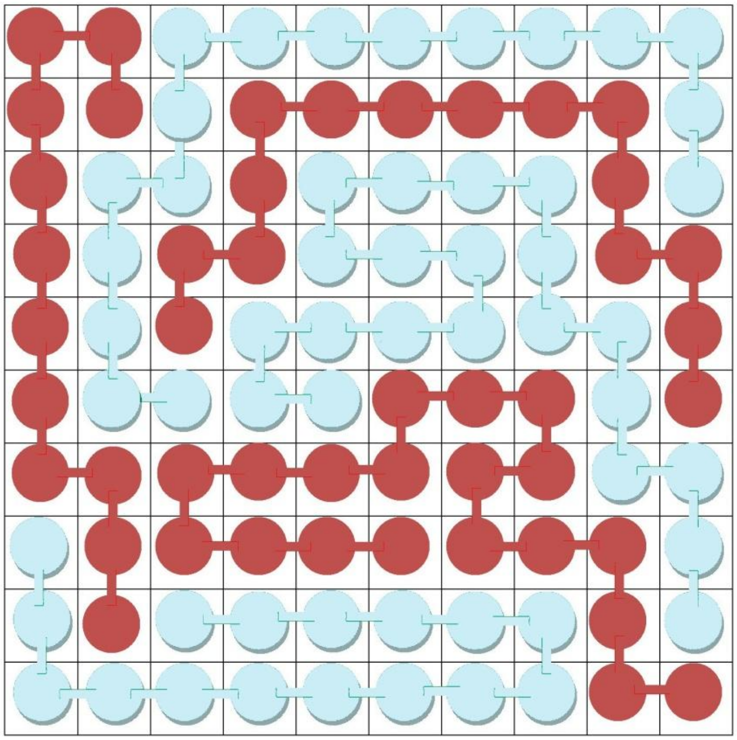

Figure 2.2 Schematic representation of the simulation cell, lattice sites (smaller squares), atoms (circles), bonds (lines connecting circles) and polymer molecules (sequences of connected circles). There are 6 chains of two different polymers (shown by dark and light colors)

The following assumptions are made in the lattice theory to treat polymer mixtures:

1. Molecules mix randomly
2. The total volume of the system and volume of lattice sites are equal
3. Molecules of a given type are indistinguishable
4. The only contribution to possible states are transitional configurations

For the case of polymer mixtures, Flory[49] obtained the total number of configurations on a lattice and presented the following expression for the mixing entropy of polymer blends:

$$\Delta S_{mix} = -k[(N_A/x_A) \ln\varphi_A + (N_B/x_B) \ln\varphi_B] \qquad 2.18$$

In which x_A and x_B are the number of segments in each branch of polymer A and B and φ_A and φ_B are volume fractions of A and B sites in the lattice and can be obtained using the following equations:

$$\varphi_A = N_A/(N_A + N_B) \text{ and } \varphi_B = N_B/(N_A + N_B) \qquad 2.19$$

To find enthalpy of mixing, we consider that a lattice site has z adjacent cells (z is 4 in 2D and 6 in 3D lattices). The probability of having A in the adjacent cells is proportional to φ_A and having B is proportional to φ_B. The following expression can be obtained for enthalpy of mixing

$$\Delta H_{mix} = z\, N_t\, [\varepsilon_{AB} - 1/2(\varepsilon_{AA} + \varepsilon_{BB})]\ \varphi_A\ \varphi_B \qquad 2.20$$

where ε_{ij} represents enthalpic interactions between i and j species.

The Flory-Huggins parameter is defined as:

$$\chi = \frac{z}{kT}\left[\varepsilon_{AB} - \frac{1}{2}(\varepsilon_{AA} + \varepsilon_{BB})\right] \qquad 2.21$$

χ represents enthalpic interactions between the components. Substituting χ into equation 2.20 results:

$$\Delta H_{mix} = N_t kT\chi\ \varphi_A\ \varphi_B \qquad 2.22$$

Substitution of enthalpy and entropy of mixing into the equation [free energy of mixing]:

$$\Delta G_{mix} = N_t kT\ [\chi\varphi_A\varphi_B + \varphi_A/x_A\ ln\varphi_A + \varphi_B/x_B\ ln\varphi_B] \qquad 2.23$$

For polymeric mixtures, the mixing entropy contribution to the mixing free energy vanishes because each polymeric molecule contains a large number of repeating units (x_i in equation 2.23 is big and $\varphi_i/x_i\ ln\varphi_i$ terms approach to zero) and hence $\Delta G_{mix} = \Delta H_{mix}$ so:

$$\Delta G_{mix} = \Delta H_{mix} = N_t kT\ [\chi\varphi_A\varphi_B] \qquad 2.24$$

$$\chi = \frac{\Delta H_{mix}}{N_t kT\varphi_A\varphi_B} \qquad 2.25$$

Based on the laws of thermodynamics:

$$\Delta H = U + \Delta(PV) \qquad 2.26$$

Where E is the internal energy of the system, P is pressure and V is the system volume. In the lattice model it is usually assumed that the change of volume on mixing is zero thus $\Delta H = \Delta E$ so:

$$\chi = \frac{\Delta E_{mix}}{N_t kT \varphi_A \varphi_B} \qquad 2.27$$

2.4 Thermodynamics of block copolymer systems

2.4.1 Theoretical treatment of block copolymer systems

Krause[50-53] is one of the pioneer researchers in the theoretical explanation of block copolymer thermodynamics. Krause's approach deals only with the development of an expression for the critical interaction parameter (χ_{cr}) in which the phase separation between blocks will occur.

In the first work[50], Krause assumed that all the copolymers have the same molecular weight and the same average composition but there was no limitation in the type of the block copolymer (A-B, A-B-A or A-B-A-B). Moreover, it was assumed that phase separation will happen completely meaning that after the phase separation the volume available for each block is equal to its volume fraction while before phase separation it is equal to the total volume of the system. The most important assumption in her work was ignoring boundary effects between phases of blocks. She developed the following expressions for the entropy, enthalpy and χ_{cr}:

$$\Delta H_{mix} = -\left(\frac{kTV}{V_r}\right)\varphi_A \varphi_B \chi_{AB} \qquad 2.28$$

$$\Delta S_{mix} = k\ (\varphi_A \ln]\ \varphi_A + \varphi_B \ln[(\varphi_B) \qquad 2.29$$

$$(\chi_{AB})_{cr} = -\left(\frac{V_r}{V_A n_A \varphi_B}\right)[\varphi_A \ln \varphi_A + \varphi_B \ln \varphi_B] \qquad 2.30$$

In which χ_{AB} is the interaction parameter, φ_i is the volume fraction of i, V is the volume of the system, V_i is the volume of repeat unit of i and n_i is the number of i units in each block copolymer molecule. Blocks of the copolymer will phase separate when $\chi_{AB} > (\chi_{AB})_{cr}$

Krause then compared results obtained from these expressions with the χ_{cr} for homopolymers and concluded that two homopolymers are more miscible as separate molecules than when they are linked into a block copolymer molecule. This means that block copolymers will phase separate in a bigger range of interaction parameter.

However, Meier[54] in a theoretical treatment of microphase separation in diblock copolymers in which surface free energies between microphases are treated as significant parameters, predicts that A-B block copolymers will show microphase separation at higher degrees of polymerization per block than the corresponding homopolymers at the same X_{AB} which contradicts Krause's predictions.

In 1970, Krause[51] published another paper in the completion of her previous work in which surface free energy was taken into account. The following expressions were developed:

$$\Delta H_{mix} = -\left(\frac{kTV}{V_r}\right)\varphi_A\varphi_B\chi_{AB}\left(1-\frac{2}{z}\right) \qquad 2.31$$

$$\Delta S_{mix} = k\ (\varphi_A \ln]\ \varphi_A + \varphi_B \ln[\![\varphi_B) - 2(m-1)\left[\frac{\Delta S_{dis}}{R}\right] + \ln(m-1) \qquad 2.32$$

$$(\chi_{AB})_{cr} = \left(\frac{zV_r}{(z-2)V_A n_A \varphi_B}\right)\left[-\varphi_A \ln \varphi_A - \varphi_B \ln \varphi_B + 2(m-1)\left[\frac{\Delta S_{dis}}{R}\right] - \ln(m-1)\right] \qquad 2.33$$

In which z is the lattice coordination number and $\Delta S_{dis}/R$ is the entropy lost when one segment of a polymer molecule is immobilized due to the connection with one segment of another block in the interface between blocks. Krause used the expression developed by Flory for this term:

$$\frac{\Delta S_{dis}}{R} = \ln\left[\frac{z-1}{e}\right] \qquad 2.34$$

in which *e* is the base of the natural logarithm.

The developed expression for the $(\chi_{AB})_{cr}$ predicted the phase behaviour of block copolymer is some cases[55] while it yielded erroneous results in some others.[53]

Another analysis of the block copolymer morphology was done by Meier.[54] In the first stage of the work, Meier assumed the domains to be spheres of block A (which has much lower volume fraction) embedded in the matrix of B component. The following assumptions are made in the treatment of block copolymers:

- Domains of the blocks are pure and only in the boundary of the domains are the two blocks mixed.
- A and B segments are equal in size.
- The polymers are amorphous.
- The block molecular weights of the components are uniform.

Meier evaluated entropy and enthalpy changes when the block copolymer phase separated from a random mixture of blocks into pure domains of A and B. The main idea behind the Meier derivation is that he avoided the calculation of entropy decrease due to the A and B blocks being constrained to their own boundaries using lattice calculation. Instead, he used diffusion equations to generate the applicable chain statistics.

The first problem to address was the prediction of the domain size as a function of the chain dimensions. To predict this value, they developed an equation for the number density of segments as a function of r (position in the domain) for different values of $(\sigma_A l^2)^{1/2}/R$ (chain dimensions to domain size ratio) in which σ_A is the number of A segments in the block, l is the statistical segment length of A and R is the domain size. In the real sample, the density of segments of A within A domain is constant and decreases sharply to 0 in the boundary. However, Meier could not find any value for $(\sigma_A l^2)^{1/2}/R$ which yields a constant density using the above mentioned equation. They suggested that in the real sample there are chain perturbations that smooth out the variations in segment density that occur for purely random-flight statistics. To deal with this issue, Meier minimized the absolute value of the of the density difference and obtained $R = 4/3(\sigma_A l^2)^{1/2}$ for the domain size.

An equation between domain size and block copolymer weight should be derived. The following correlation between unperturbed chain length and molecular weight is known:

$$\langle \sigma l^2 \rangle_o^{\frac{1}{2}} = KM^{\frac{1}{2}} \qquad 2.35$$

If the ratio of perturbed to unperturbed chain dimension is presented by α, then we may write:

$$R = \frac{4}{3}\alpha K M_A^{\frac{1}{2}} \qquad 2.36$$

where K is a characteristic of the constituent blocks. The only unknown parameter in equation 2.36 is a which should be defined to determine the domain size (R).

To derive an expression to find a, Meier derived an expression for the Gibbs free energy of domain formation (ΔG_d) as a function of a and set $d(\Delta G_d)/d\alpha$ to zero to find a. to obtain ΔG_d, entropy, enthalpy and surface free energy terms must be defined. Three phenomena contribute to the entropy decrease in block copolymers:

1) Placement entropy (ΔS_p): A-B junction must be in the interface between domains which decreases the available configurations.
2) Restricted volume entropy (ΔS_v): A and B segments are limited to their own domains.
3) Elasticity entropy (ΔS_{el}): Perturbation of chains from their random flight value which also decreases the entropy.

There are two limits for the placement entropy. The upper limit is when we assume that all sites within a cell have the same probability. Obviously this assumption is not completely true since chain origins have the tendency of avoiding each other. Nevertheless:

$$(\Delta S_p)_{max} = kN_{AB}\ln\left(\frac{3\sigma_A \Delta R}{(\sigma_A + \sigma_B)R}\right) \qquad 2.37$$

In which $N_{AB} = \sigma_A + \sigma_B$ and ΔR is the interface thickness. And the minimum limit for the placement entropy:

$$(\Delta S_p)_{min} = -kN_{AB}\ln(\sigma_A + \sigma_B) \qquad 2.38$$

The minimum case occurs when only one site per cell can be occupied by the junction.

Restricted volume entropy is calculated using diffusion equations instead of lattice theory and the interface is treated as completely absorbing barrier for both components. The final expression for entropy loss is as follows:

$$\Delta S_v = N_{AB}k\left[\ln P(\sigma_A; r', r < R) + \ln P(\sigma_B; r', r > R)\right] \qquad 2.39$$

In which $P(\sigma_A; r', r < R)$ is the probability of having all A segments inside the boundary with R dimension and $P(\sigma_B; r', r > R)$ is the probability of having all B segments outside such boundary. The following expression can be used to evaluate these probabilities:

$$P(\sigma_A; r', r < R) = 2\sum_{i=1}^{\infty}(-1)^{i+1} j_0\left(\frac{i\pi r'}{R}\right)\exp\left\{-\frac{i^2\pi^2\sigma_A l^2}{6R^2}\right\} \qquad 2.40$$

$$P(\sigma_B; r', r > R) = 1.0 - \left({}^{R}/_{r'}\right)\mathbf{Erfc}\left(\frac{3}{2\sigma_B l^2}\right)^{\frac{1}{2}}(r' - R) \qquad 2.41$$

In which $j_0(z)$ is spherical Bessel function of order 0 and Erfc(z) is the complementary error function:

$$\mathbf{Erfc}(z) = 1 - \mathbf{Erf}(z) \qquad 2.42$$

Where Erf(z) is the error function.

Finally, elasticity entropy can be evaluated using:

$$\Delta S_{el} = -\frac{3}{2}N_{AB}k(a^2 - 1 - 2\ln a) \qquad 2.43$$

Where a is the ratio of perturbed to unperturbed end-to-end distances.

The second contribution to free energy is due to enthalpy change from a random mixture of blocks to pure domains of A and B. This enthalpy change is equal to the negative of the heat of mixing of a simple mixture of the component blocks of the block copolymer:

$$\Delta H = N_{AB}kT\chi\left[\frac{\sigma_A}{\sigma_A + \sigma_B}\right] \qquad 2.44$$

In which χ is the Flory-Huggins parameter and σ_i is the number of i segments in the lattice.

The third contribution to free energy of mixing is from surface free energy which can be obtained from the following expression:

$$G_s = \frac{9}{4}\frac{N_{AB}M\ {}_A^{\frac{1}{2}}\gamma}{\bar{A}\rho a K} \qquad 2.45$$

In which M_A is the molecular weight of block A, γ is the interfacial tension (free energy of mixing in the interface of one domain), Ā is Avogadro's number, ρ is the density, a is the perturbation ratio and K is:

$$\mathrm{K} = \langle \sigma l^2 \rangle_o^{1/2} / \mathrm{M}^{1/2} \qquad 2.46$$

Free energy of domain formation which is the summation of all those five contributions is as follows:

$$\frac{\Delta G_d}{N_{AB}kT} = \ln\left(\frac{\sigma_A+\sigma_B}{3\sigma_A}\right)\left(\frac{R}{\Delta R}\right) - \ln P\left(\sigma_A; r', r < R\right) - \ln P\left(\sigma_B; r', r > R\right) + \frac{3}{2}\left(a^2 - 1 - 2\ln a\right) + \frac{9M_A^{1/2}\gamma}{4aK\bar{A}\rho kT} - \chi\sigma_A/(\sigma_A + \sigma_B) \qquad 2.47$$

As mentioned above, the goal of the free energy of domain formation calculation is evaluate the degree of chain perturbation when the block copolymer undergoes phase separation. The chain perturbation ratio appears in term relating to the interfacial energy and the elastic free energy. The equilibrium value of a is obtained by differentiation of ΔG_d with respect to a. The value of a corresponding to minimum free energy of domain formation is:

$$a^3{}_m - a_m = \frac{3M_A^{\frac{1}{2}}\gamma}{Kk\rho\bar{A}T} \qquad 2.48$$

Then the domain size in case of spherical domains can be obtained using equation 2.36.

Meier commented that the comparison between the domain sizes obtained from this equation and the experimental results is rather difficult due to lack of interfacial tension data for polymer systems which is needed in perturbation ratio (a) evaluation. However, he found that the equation yields in reasonable values of domain size.

In a later work, Meier calculated free energy of phase separation for 3 different structures: spherical, cylindrical and lamellar and determined the most stable structure for different compositions.

2.4.2 Experimental studies

Theoretical studies in diblock copolymer morphology, even though important, were not sufficient. Experimental studies have had an important role in the recognition and characterization of the different structures for block copolymers. The most detailed phase diagrams for a variety of copolymers have been developed using results from experimental studies.

Based on the results of experimental studies the morphology of undiluted diblock copolymers is determined by three factors: the A-B segment-segment Flory-Huggins interaction parameter (χ), the volume fraction of constituent blocks in the polymer (φ_A and φ_B) and the overall degree of polymerization (N).

Phase diagrams of diblock copolymers are divided into three regimes: weak segregation limit (WSL), intermediate segregation region (ISR) and strong segregation limit (SSL) depending on the combined parameter, χN. [56] In the WSL, the composition in different regions deviates slightly from the average value. This means that we do not have domains of pure A or B blocks and the two blocks are intimately mixed at the microscopic level.[57] For copolymers with infinite length ($N \to \infty$), as the χN value approaches 10, individual chains are significantly extended from their unperturbed Gaussian dimensions which is considered as a signal for crossover from WSL to ISR.[58] As the χN value approaches roughly 50 to 100,[56] domains of pure blocks with sharp interfaces start to appear which is characteristic of the SSL. Three regimes in block copolymer phase behavior are schematically illustrated in the Figure 2.3:

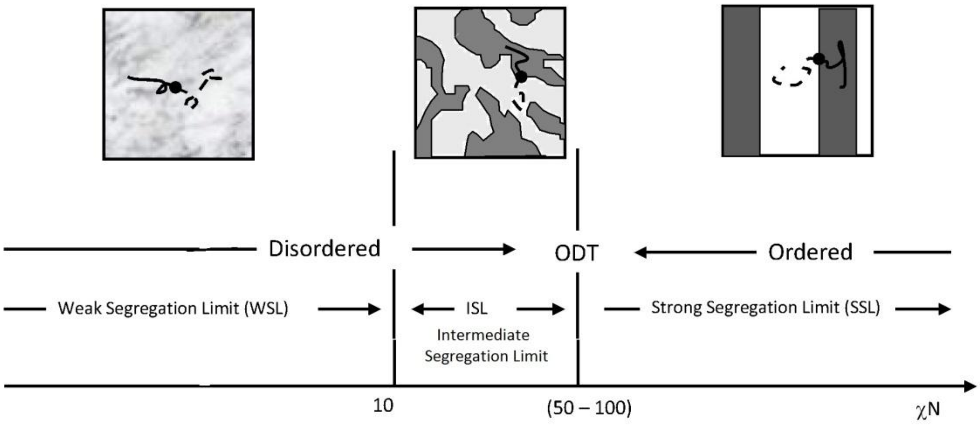

Figure 2.3: Illustration of different states of segregation in diblock copolymer.

Fredrickson and Helfand[60] formulated order-disorder transition χN as a function of the degree of polymerization for symmetric diblock copolymers with finite degree of polymerization:

$$(\chi N)_{ODT} = 10.495 + 41.0\,\overline{N}^{-\frac{1}{3}} \qquad 2.49$$

where $\overline{N} = Na^6v^{-2}$. a and v are the statistical segment length and volume.

Flory-Huggins interaction parameter decreases with temperature increase and in most of the cases, there is linear correlation between χ value and reciprocal temperature:

$$\chi \approx \alpha T^{-1} + \beta,\ \alpha > 0 \qquad 2.50$$

Block copolymers can form various structures in the strong segregation limit depending on the volume fraction of the constituent blocks. A typical phase diagram is shown in Figure 2.4. Spherical structure is observed when the volume fraction of one block is much less than the other block. This type of nanostructure is not suitable for PSC active layer and this region should be avoided. As the volume fraction of the block increases, cylindrical, bicontinuous, perforated and lamellar structures appear. It must be noted that phase diagrams are not generic and transition volume fraction between various morphologies depends on the molecular structure of the blocks.

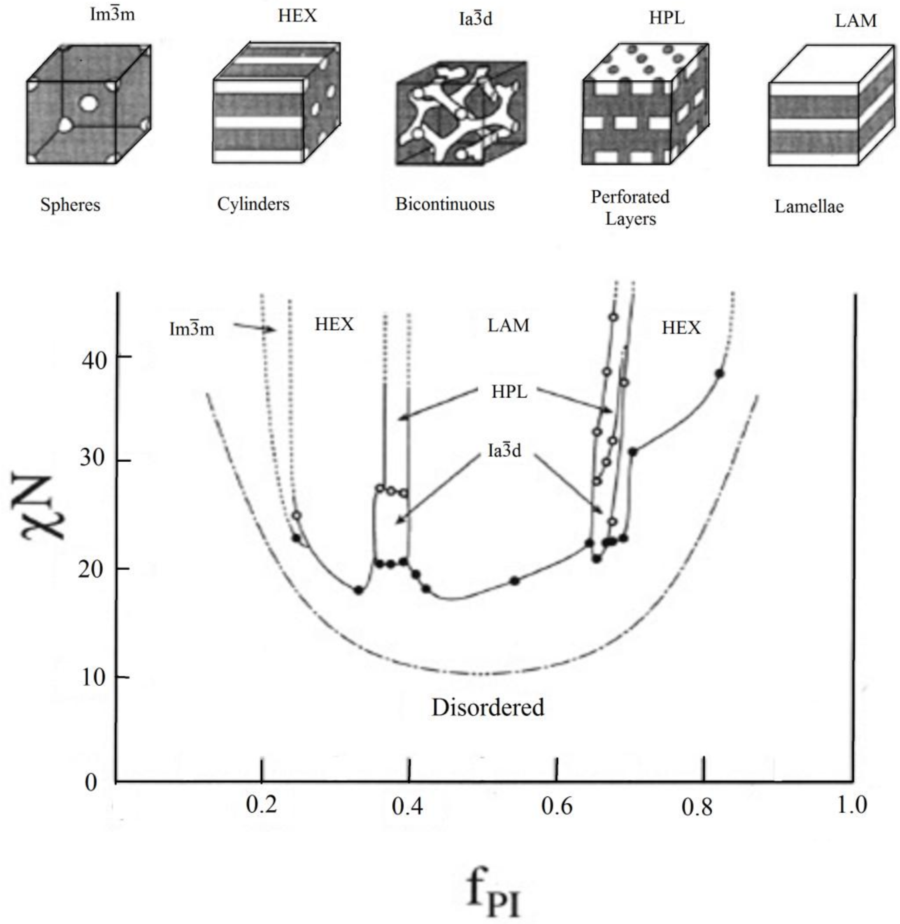

Figure 2.4: The upper panel shows five different common nanostructures and phase diagram of polyisoprene-polystyrene is shown in lower panel. f_{PI} is the volume fraction of polyisoprene. (Reprinted with permission from reference 61, Copyright 1995 American Chemical Society)

Since volume fraction of blocks and the overall degree of polymerization can be readily controlled while synthesizing the block copolymer, the most important factor which determines nanostructure and degree of self-segregation is Flory-Huggins interaction parameter.

Chapter 3

Foundations of molecular dynamics simulations

In the current work for the calculation of the Flory-Huggins parameter, we need to determine the potential energy and density of the pure polymer blocks and polymer blends. Molecular Dynamics simulations are used for this purpose which will be discussed briefly in this chapter.

3.1 Introduction

Computer simulations are carried out to understand properties of pure materials or microscopic interactions between different molecules. Two different techniques of computer simulations are Monte Carlo (MC)[62] and Molecular Dynamics[63] (MD). In the Monte Carlo technique, a set of different samples of the system is created and the average of their properties is calculated to predict the behaviour of the macroscopic system. However, in the molecular dynamics technique the evolution of the system in time space from initial conditions to the final equilibrium state is evaluated. The obvious advantage of Molecular Dynamics simulations over Monte Carlo technique is that the time-dependent information of the system is available and the evaluation of the time-dependent properties such as transport coefficients and rheological properties is possible.

3.2 Equations of Motion

The Main idea behind the Molecular Dynamics simulations is to solve Newton's equations of motion for a system of n particles and obtain velocities and positions of those particles in the phase space. The Newtonian equation of motion is as follows:

$$F_i(t) = m_i a_i(t) \qquad 3.1$$

Where F is the force acting on particle i, m is the mass and a is the acceleration of the particle i.

The force on atom i can be computed directly from the derivative of the potential energy U with respect to the coordinate **r**:

$$F(t) = \frac{\partial U(r,t)}{\partial r} \qquad 3.2$$

The potential energy of particles can be determined using forcefields which will be discussed in section 3.4. Classical equations of motion are deterministic meaning that having initial values of velocities and positions in time t_0, positions and velocities of all particles in other times can be determined. Finite difference methods can be used to solve equations of motion in discrete time steps to yield the velocity and positions of all particles. In the given time, the positions and velocities of all particles in the system are stored in a *trajectory*.

Integrating Newton's equations of motion allows us to explore the constant-energy surface of a system. However, density calculation is performed at constant pressure and potential energy calculation must be performed at constant volume. Under these conditions, the total energy of the system is no longer conserved and extended forms of molecular dynamics are required. These extended forms or *ensembles* will be discussed in section 3.7.

3.3 Amorphous Cell Construction

The first step in Molecular Dynamics simulation is to build the simulation box which is also called *Amorphous Cell*. In this section, the method which is used for amorphous cell construction is discussed briefly.

This process is the growing of polymer molecules inside a box with a known volume. The process starts with one particle and then grows the rest of the molecule by specifying bonds and positions of the next atoms. For rigid molecules (typically small molecules) with known bond angles and bond lengths there is only a single way of growing the molecule. However, for molecules with flexible backbone like polymers, torsion angles are degrees of freedom since there is not a specified value for them and the potential energy distribution as a function of torsion angle is such that there are several possible values for a given angle.

To minimize the simulation times in the later stages of calculation, molecules in the constructed cell must be as close as possible to their minimum energy states. At room temperature, bond lengths and angles have a single known value and they can be set fixed during amorphous cell calculation leaving torsion angle to be the single variable parameter that should be determined. Rotational Isometric Theory (RIS)[64-66] has been used extensively in literature to find discrete values of torsion angles associated with minimal energies (minimal energy states). The second approach is to consider a range of possible angles near the RIS minimal states. The population of substates (or the probability that a specific structure is used in the amorphous cell construction) is determined using the Boltzmann distribution. Based on the Boltzmann distribution, the probability profile of torsion angles depends on their energy level and temperature: at lower temperatures the RIS state with the minimum energy is the only possible state but as temperature increases, the distribution range becomes broader. A sample conformation energy map and probability distributions of torsion angle at two different temperatures, 600 K and 150 K, are shown in Figure 3.1. Probability associated with substate i (P_i) is calculated from the Maxwell-Boltzmann distribution:

$$P_i = \frac{g_i \exp\left(-\frac{E_i}{RT}\right)}{\sum g_j \exp\left(-\frac{E_j}{RT}\right)} \qquad 3.3$$

Where E_i is the energy level of the substate i, T is the temperature, R is the ideal gas constant and g_i is the degeneracy factor.

In this example, RIS torsion angles are π/3, 5π/4 and 5π/6. At 600K, a range of torsion angles are possible while at 150K, the only possibility is the torsion angle of 5π/4.

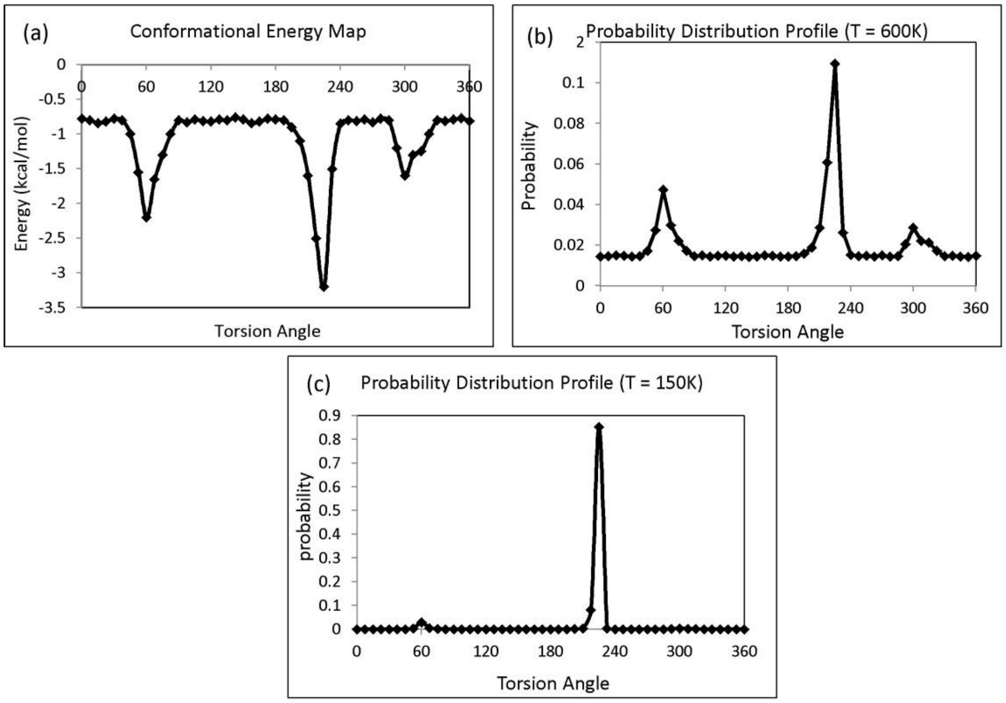

Figure 3.1: (a) conformational energy map, (b) probability distribution at 600K and (c) probability distribution at 150K.

After the determination of torsion angles, amorphous cell construction process starts by placing an atom in a random place and then growing segments inside the box with a stepwise process using known values of bond length, bond angle and torsion angles. It is possible that in some point, the calculated route for the next bond/atom is already occupied. In this case, the constructor reconstructs several bonds using different values of torsion angles to circumvent the obstacle. Having a range of possible torsion angles instead of single values facilitates amorphous cell construction as it gives more freedom in growing chains around obstacles.

During the construction procedure the constructed structure must be checked to avoid ring spearing if the structure contains close rings. This is because any change during the subsequent simulation steps is impossible if one branch crosses through a ring.

To avoid amorphous cell construction failure, usually the density of the constructed cell is less than the experimental value because a higher density means that it will be hard to grow the last molecules or parts of the chain due to a very limited space. NPT simulations are used to compress the constructed cell to its equilibrium density.

3.4 Forcefields

3.4.1 Developing a forcefield

There are two important aspects to each forcefield: the mathematical form and the value of the parameters.

The potential energy of a molecule can be written as:

$$E = \sum_{bonds} E_{stretch} + \sum_{angles} E_{bending} + \sum_{dihedrals} E_{tortion} + \sum_{pairs} E_{nonbond} \qquad 3.4$$

A brief description of each term is as follows:

- Bond stretching potential: molecules can be approximated as balls (atoms) that are held together by springs (chemical bonds). Based on the Hooke's law the energy of a spring has a linear correlation with the length change square:

  $$E_{bond} = k_{bond}(l - l_{eq})^2 \qquad 3.5$$

  k_{bond} is the constant of proportionality in the equation and the bigger k_{bond} means stiffer bond/spring which resists more against being stretched. l is the current length of the bond/spring and l_{eq} is the equilibrium length of the bond which corresponds to zero of potential energy. In the case of this example, bond potential is approximated by quadratic form but in more accurate forcefields, cubic term might be included as well.

- Angle bending potential: The change in the potential of a molecule when the angle between three atoms (A-B-C) changes can be deemed proportional to the square of the change in the angle:

  $$E_{angle} = k_{angle}(a - a_{eq})^2 \qquad 3.6$$

  Where K_{angle} is the proportionality constant, a is the size of the angle when distorted; and a_{eq} is the equilibrium (natural) size of the angle which corresponds to zero potential energy.

- Dihedral torsion potential: In a molecule, the torsion angle is defined for four consecutive atoms (A-B-C-D) as the angle between the A–B bond and the C–D bond as viewed along the B–C bond. The potential of a torsion angle cycles every 360 degree meaning that the potential of the θ is equal to $\theta+360$ so dihedral torsion potential must have the *sine* or *cosine* form:

  $$E_{torsion} = k(1 + \cos(n\varphi)) \qquad 3.7$$

  Where k is the proportionality constant and φ is the torsion angle.

- The non-bonded pairs potential: The potential energy change with the atomic distance for atoms that are bonded is counted for in the *bond stretching potential* and for the atomic pairs that are bonded to a common atom is counted for in the *angle bending potential* so *non-bonded pair* is defined as a pair of atoms which are not directly bonded (A-B) or are not bonded to a common atom (A-X-B). Non-bonded term included interactions between atoms that are separated by more than one atom on the same molecule or atoms that are on the separate molecules.

The potential energy curve for two nonpolar non-bonded atoms has the general form shown in figure 3.2:

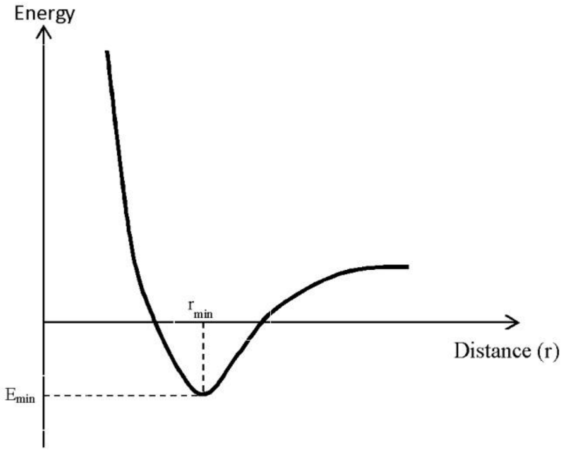

Figure 3.2: Non-bonded potential energy versus distance

A simple way to approximate this is by the so-called Lennard–Jones 12-6 potential:

$$E_{nonbond} = 4\varepsilon\left[\left(\frac{\sigma}{r}\right)^{12} - \left(\frac{\sigma}{r}\right)^{6}\right] \qquad 3.8$$

where r is the distance between the centers of the nonbonded atoms or groups, ε is the minimum potential energy attainable by the system (E_{min}) which occurs when r is equal to r_{min} (as indicated in figure 3.2). r_{min} is the sum of the van der Waals radii of atoms: $r_{min} = r_A + r_B$.

Setting dE

/dr = 0 we find that:

$$\sigma = 2^{-1/6}\, r_{min} \qquad 3.9$$

It is worth mentioning that the above mathematical expression for different terms in the forcefield are just examples and different forcefields might have different mathematical forms.

3.4.2 Parameterizing a forcefield

The second step is to parameterize the forcefield by assigning numerical values for k_{bond}, k_{angle}, l_{eq} and a_{eq} etc., into the equations to give expressions that we can actually use. The process of finding these numbers is called *parameterizing the forcefield*. The set of molecules used for parameterization, perhaps 100 for a good forcefield, is called the *training set*.[67] A forcefield can be parameterized using experimental results (empirical parameterization) or by high-level *ab initio* or density functional calculations or by a combination of both approaches. For instance, k_{bond} could be obtained experimentally from IR spectra, as the stretching frequency of a bond depends on the force constant (and the masses of the atoms involved)[68], and l_{eq} could be derived from X-ray diffraction, electron diffraction, or microwave spectroscopy.

The result of many experimental and calculational data is used to gain the best fit which is used to parameterize the forcefield. These parameters are different for different atoms and even for different kind of bonds between the same atoms like single and double bonds.

3.5 Interaction Computations

In computer simulations, it is impossible to take into account all the details of the system due to the limited storage and computation capacity. One of the most important steps in setting up a computer simulation is to define important parameters of the system that must be taken into account and those details that can be ignored without serious errors.

In this section two techniques are discussed to optimize the pair selection and minimize computation and storage requirements while having good accuracy.

3.5.1 All Pairs Method

This is the simplest method and all interactions between all particle pairs of the system, regardless of their distance, are assessed. Calculations in this method are from order N_m^2 where N_m is the number of the particles in the system. In this technique computational cost increases dramatically with the size of the system.

3.5.2 Cell Subdivision Method

In this method a cut-off interaction length r_c is selected so that interactions between particles with distance more than r_c are negligible. Simulation cell is divided into a lattice of subcells with r_c dimensions. In order to calculate the interactions for a given particle, only particles within the lattice subcells immediate to the given subcell are considered (26 and 8 neighboring subcells in 3D and 2D models respectively). The calculation order is reduced to N_m using this technique. For this technique to be useful, the dimension of the simulation cell must be bigger than 3 r_c. The method is represented schematically in figure 3.3.

3.5.3 Neighbor-list Method

As mentioned in the cell subdivision method, we are interested only in the interactions between particles that are less than r_c apart. In the cell subdivision method only $\frac{4}{3}\pi r^3 / 27r^3 = 0.16$ of particles considered in 3D and $\pi r^2 / 9r^2 = 0.35$ of the particles in 2D lie in the r_c distance. In the neighbor-list method, a list of the particles with distance less than r_c is determined and interactions with these particles are calculated. This list must be updated for every particle each timestep.

The importance of the cell-subdivision and neighbor-list methods in the reduction of the computational costs is shown in figure 3.3.

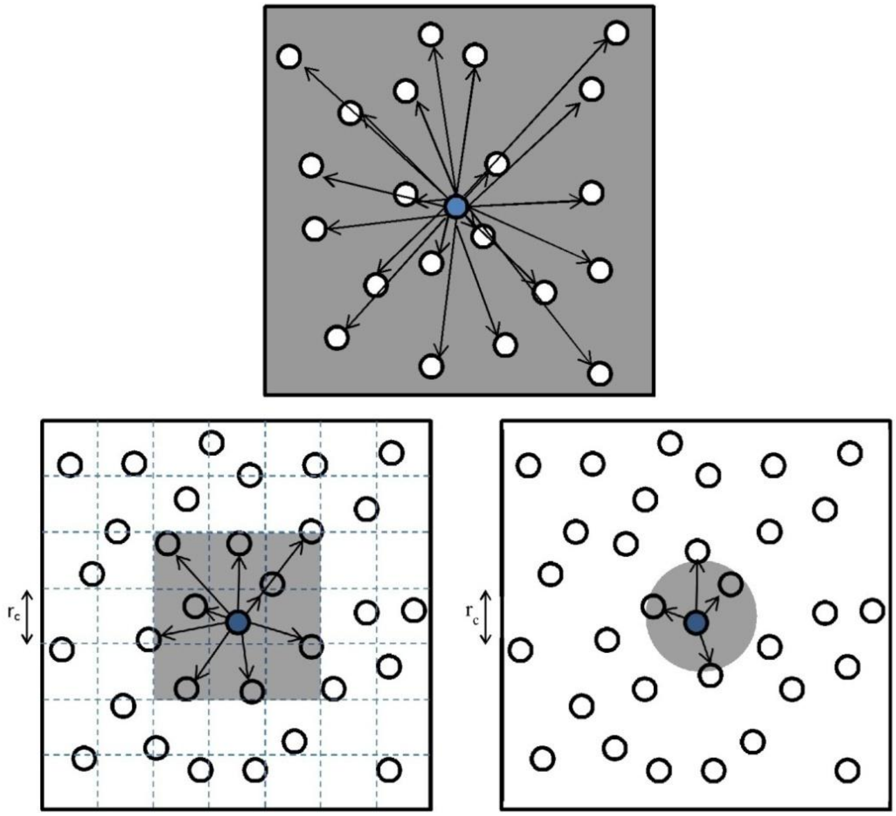

Figure 3.3: Different approaches for the interaction computation. The filled circle depicts the designated particle in all three cases and the shaded area indicates the region that interactions are taken into account. Every interaction is shown with an arrow.

3.6 Integration techniques

As mentioned in the introduction section, molecular dynamics solves Newtonian equations for a system of N particles. Finite difference algorithms such as Verlet Velocity, ABM (Adams-Bashforth-Moulton) and Runge-Kutta are usually used for this purpose. In this section these techniques will be discussed briefly.

Finite difference technique is based on the calculation of the velocity and position of every particle in time $t+\Delta t$ using the properties in the time t. These calculations start with having the velocity and position of every particle in time 0 (*initial conditions*). In MD simulations, position of the particles is obtained from input file however; velocities are randomly assigned for the particles so that the temperature of the system is equal to the setpoint. This implies that different runs on the same machine will not have exactly the same results.

There are two types of integrators: Leapfrog-type methods and predictor-corrector methods.

3.6.1 Leapfrog-type methods

In these methods values of position, velocity and acceleration (calculated from pair potential) in the previous step are used to calculate trajectory at the current time. Leapfrog-type algorithms are essentially time-reversible in nature so it provides better energy conservation with strongly divergent U-type potentials at larger runtime lengths. Moreover, these methods require minimal storage space and hence are suitable for extremely large-scale studies where storage can become an important issue. Three Leapfrog-type algorithms are described below briefly:

3.6.1.1 Leapfrog method:

This is one of the simplest methods of solving Newtonian equations. In this method velocity and position is updated at interleaved time points. For example velocity is updated at time t and position is updated at time $t + {}^{\Delta t}/_{2}$. Algorithms of this method are as follows:

$$x_t = x_{t-\Delta t} + v_{\left(t-{}^{\Delta t}/_{2}\right)}\Delta t \tag{3.10}$$

$$a_t = \frac{F(x_t)}{m} \tag{3.11}$$

$$v_{\left(t+{}^{\Delta t}/_{2}\right)} = v_{\left(t-{}^{\Delta t}/_{2}\right)} + a_t\Delta t \tag{3.12}$$

3.6.1.2 Verlet integrator:[69]

Verlet integration was used by Carl Stormer to compute the trajectories of particles moving in a magnetic field (hence it is also called Störmer's method) and was popularized in molecular dynamics by French physicist Loup Verlet in 1967. The Verlet integration algorithm is as follows:

$$x_{(t+\Delta t)} = 2x_t - x_{(t-\Delta t)} + a_t \Delta t^2 \qquad 3.13$$

$$ma_t = F(x_t) \qquad 3.14$$

$$v_{(t+\Delta t)} = \frac{x_{(t-\Delta t)} - x_t}{\Delta t} \qquad 3.15$$

3.6.1.3 Verlet Velocity Integrator:[70]

This method is a combination of Verlet and Leapfrog methods which is commonly used in Molecular Dynamics simulations. The Verlocity Verlet algorithm is as follows:

$$x_{(t+\Delta t)} = x_t + v_t \Delta t + \frac{\Delta t^2 a_t}{2} \qquad 3.16$$

$$a_{(t+\Delta t)} = \frac{F\left(x_{(t+\Delta t)}\right)}{m} \qquad 3.17$$

$$v_{(t+\Delta t)} = v_t + \frac{\Delta t}{2\left(a_t + a_{(t+\Delta t)}\right)} \qquad 3.18$$

3.6.2 Predictor-corrector Methods

Predictor-corrector methods are executed in two steps: in the first step a rough approximation of the answer is determined and in the second step the initial approximation is corrected. Because of the greater flexibility and potentially higher local accuracy, predictor-corrector methods tend to be suited to more complex problems such as rigid bodies or constrained dynamics, where greater accuracy at each timestep is desirable.

3.6.2.1 Adams-Bashforth-Moulton integrator:

The algorithm for this method is as follows:

$$x_t{}^{Predicted} = x_{(t-\Delta t)} + \frac{\Delta t}{24}\left(55v_{(t-\Delta t)} - 59v_{(t-2\Delta t)} - 37v_{(t-3\Delta t)} - 9v_{(t-4\Delta t)}\right) \quad 3.19$$

After this step $v_t{}^{predicted}$ is evaluated using $x_t{}^{Predicted}$ and the corrector is:

$$x_t{}^{Corrected} = x_{(t-\Delta t)} + \frac{\Delta t}{24}\left(9v_t + 19v_{(t-\Delta t)} - 5v_{(t-2\Delta t)} - v_{(t-3\Delta t)}\right) \quad 3.20$$

Finally $v_t{}^{corrected}$ is evaluated using $x_t{}^{corrected}$.

3.6.3 Integrator selection criteria

Several criteria are used to choose the appropriate integrator:

- Memory usage: Whenever dealing with big systems, memory usage of integrators is very important. Memory usage of a method mainly depends on the number of previous steps must be stored and used to calculate the trajectory of the system in the later steps.

- Speed: speed of every algorithm depends on the step length and calculation speed of every step. The longer step means that the total simulation time will be less. On the other hand, the error involved in the finite-difference integration methods generally depends on the time step length. Shorter time step will result in less error and more accuracy. Hence the choice of a particular timestep is a tradeoff between simulation time and accuracy depends on the chosen integration technique and characteristics of the system.

- Good conservation of energy: To create realistic statistical ensembles, conservation of energy must be checked in every step. Velocities of the particles in the system are usually scaled to ensure the total energy of the system is conserved.

Based on the above criteria, Velocity Verlet algorithm is the most widely used technique since it offers greater stability with relatively low computational cost. The main advantage of this algorithm over a simple Leapfrog method is that the positions and velocities are calculated for the same time which makes the calculation of potential and kinetic energy possible at the same time. Potential and kinetic energy of the system are needed to evaluate the conservation of the total energy of the system.

3.7 Various Thermodynamic Ensembles

MD studies are based on the statistical thermodynamics and they are intended to predict macroscopic properties of the system from microscopic details. To gain accurate results from a simulation, the simulation conditions must be realistic. Newtonian equations of motion conserve energy but experimental conditions in which macroscopic properties are measured are not always in constant energy. For instance density measurement is performed in constant temperature and pressure. The system can exchange heat with the environment so the total energy is not necessarily conserved. To implement such conditions in the simulation we need to use ensembles other than the conventional NVE ensemble in which the number of particles, volume and total energy of the system is constant. NVE ensemble is also referred to as *microcanonical ensemble*.

Temperature and pressure are the properties that are normally fixed during a simulation. In the NVT (*canonical ensemble*) volume and temperature of the system and in the NPT (*isothermal-isobaric ensemble*) pressure and temperature of the system are kept constant. In the next sections some methods of controlling pressure and temperature are discussed briefly.

3.7.1 Temperature Control

Temperature must be kept constant in both NPT and NVT ensembles. Temperature of a system depends on the velocity of the particles of the system so to control the temperature of a system particle velocities must be tuned. Temperature and average kinetic energy of the system are correlated using *equipartition theory*. Equipartition means "equal division" and the equipartition theory states that for a system, every degree of freedom contributes $\frac{k_B T}{2}$ to the average kinetic energy so for a system with N_f degree of freedom

$$\langle KE \rangle = \frac{N_f k_B T}{2} \qquad 3.21$$

where k_B is the Boltzmann constant. For a system of N particles the total number of degrees of freedom is $3N$-3 for periodic and $3N$-6 for nonperiodic systems. On the other hand, average kinetic energy of a system can obtained from the average of kinetic energies of the particles of the system:

$$\langle KE \rangle = \langle \sum \frac{m v_i^2}{2} \rangle \qquad 3.22$$

Where $v = \sqrt{(v_x^2 + v_y^2 + v_z^2)}$.

Hence, temperature of the system can be calculated if particle velocities are known using the combination of equation 3.21 and 3.22:

$$T = \frac{1}{N_f k_B} \langle \sum m v_i^2 \rangle \qquad 3.23$$

Equation 3.23 is used to calculate the temperature of the system. Another issue in MD simulations is to distribute particle velocities in a realistic way so that the system temperature is equal to the predefined value. In a realistic trajectory particle velocities and temperature must be correlated based on the Maxwell-Boltzmann distribution function

$$f(v) = \left(\frac{m}{2\pi k_B T}\right)^{3/2} \exp\left(-\frac{mv^2}{2k_B T}\right) 4\pi v^2 dv \qquad 3.24$$

f(v) is the probability that a specific particle within the system has the velocity between *v* and *v+dv*. In the above equation *m* is the mass of the particle, k_B is the Boltzmann constant, *T* is the temperature of the system and *v* is the velocity. Velocity distribution of hydrogen molecules in different temperatures are depicted in figure 3.4.

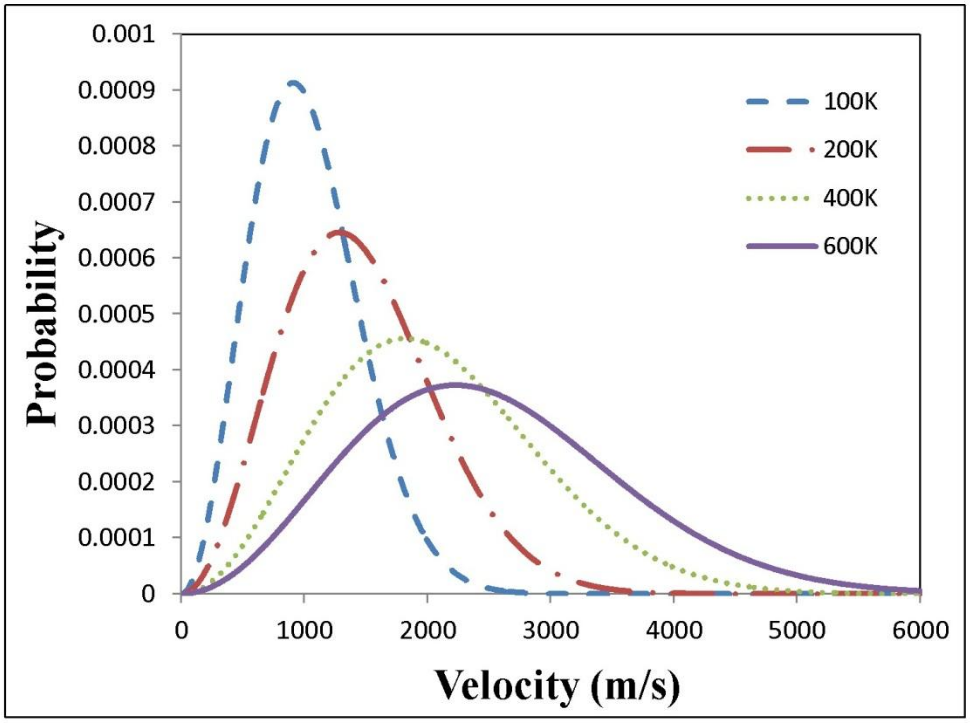

Figure 3.4: Velocity distribution probability obtained from Maxwell-Boltzmann distribution for hydrogen molecule with $m = 3.34 \times 10^{-27}$ kg. In this graph *dv* is 1m/s.

It can be seen in the above graph that the velocity of all the particles are not the same and the profile is different for various temperatures in a realistic system.

The goal of temperature control in MD simulations is not to keep the temperature constant but is to ensure that the average temperature of the system during simulation time is equal to the setpoint temperature.

3.7.1.1 Direct Velocity Scaling

This is the simplest method of controlling temperature in the system. In this method, after every few steps, the temperature of the system is calculated from the velocities of the particles of the system and these velocities are scaled by a factor so that the system temperature is exactly equal to the pre-defined value. Equation 3.25 can be used for velocity scaling:

$$v_{i,new} = v_{i,old}\sqrt{\frac{T_{target}}{T_{current}}} \qquad 3.25$$

where v_i is the velocity of particle i.

This procedure is identical to adding and subtracting energy from the system drastically so that the system temperature will change instantaneously. However in the physical systems the amount of the heat exchange to the system is limited. Moreover, this method multiplies velocity distribution by a constant value but as shown in figure 3.4, velocity distribution has different shapes in different temperatures and velocity distribution in one temperature cannot be reproduced by multiplication of velocities at other temperature with a constant value. This implies that velocity distributions produced by the velocity scaling are not realistic.

3.7.1.2 Berendsen thermostat[71]

This thermostat is a developed form of the velocity scaling in which particle velocities of the system are tuned gently by introducing a λ factor:

$$\frac{v_{i,new}}{v_{i,old}} = \lambda = \sqrt{\left[1 - \frac{\Delta t}{\tau}\left(\frac{T_{current} - T_{target}}{T_{current}}\right)\right]} \qquad 3.26$$

where Δt is the timestep length and τ is the characteristic relaxation time. Berendsen thermostat with the relaxation time equal to the timestep length is identical to the *direct velocity scaling* while a bigger τ will result in a smoother temperature control.

Direct velocity scaling and *Berendsen thermostats* are the simplest methods of controlling temperature in Molecular Dynamics simulations. However, these procedures suppress natural fluctuations of kinetic energy of the system and the produced trajectories are not realistic. Hence these methods are not suitable for simulations of dynamic properties but in the calculation of the equilibrium properties, these methods are favorable due to their simplicity.

3.7.1.3 Andersen Thermostat[72]

In the Andersen method of controlling temperature, velocities of all particles are reassigned randomly every *collision period* so that the temperature of the system is equal to the user-defined value. This method is identical to introducing stochastic forces to the system to tune the velocities of the system. This method will result in artificial trajectories and it is suitable only if the equilibrium properties are the output properties of the simulation.

3.7.1.4 Nose and Nose-Hoover Thermostats[73-75]

Since the energy of a system fluctuates in constant temperature, we need to change the NVE ensemble to introduce energy fluctuation into the system so that the average temperature of the system is constant.

The main idea behind Nose thermostat is to add an additional degree of freedom to the system by introducing additional artificial coordinates and velocities to the system Lagrangian to simulate the interaction of the system with a heat bath. This method is realistic and produces true trajectories and hence is suitable for the calculation of the dynamic properties.

3.7.2 Pressure Control

Pressure is a thermodynamic property which is defined for a system constrained in a limited volume. Pressure is usually calculated in molecular dynamics simulations from the following expression:

$$PV = Nk_BT + \frac{1}{3}\langle \sum_{i=1}^{N} \boldsymbol{r}_i \cdot \boldsymbol{f}_i \rangle \qquad 3.27$$

Where P is the pressure, T is the temperature, k_B is the Boltzmann constant, $\boldsymbol{r}_i$ is position coordinate vector and $\boldsymbol{f}_i$ is the force vector acting on the particle i.

3.7.2.1 Berendsen Barostat[71]

The pressure can be changed by changing coordinates of particles and volume of the cell in constant temperature. Berendsen is a length-scaling technique meaning that dimensions of the container and coordinates of the particles are rescaled using the μ factor: $r_i \rightarrow \mu r_i \text{ and } L \rightarrow \mu L$. The rescaling factor is calculated from equation 3.28.

$$\mu = \left(1 + \frac{\Delta t}{\tau}\gamma[P - P_0]\right)^{\frac{1}{3}} \qquad 3.28$$

where Δt is the timestep, P is the current pressure of the system and P_0 is the target pressure. τ is the *relaxation time constant* and γ is the compressibility of the system and both of these variables are defined by the user.

In this method the shape of the cell remains constant and therefore, it is not appropriate for the systems in which a shape change is expected. Moreover, length scaling uses a global scaling factor which leads to violent oscillations of pressure and, similar to the velocity scaling methods for temperature control, produces artificial trajectories and is not suitable for the calculation of dynamics properties. However, it is often used for the calculation of equilibrium properties.

3.7.2.2 Andersen Barostat[72]

In the Andersen barostat, two artificial variables are added to the system: the kinetic energy term with a user-defined mass M and the potential $P_{ext}V$ which is derived from an external pressure P_{ext} acting on the volume of the system V.

Andersen barostat, similar to Berendsen barostat, keeps the shape of the cell constant but it produces more realistic trajectories and is suitable for the calculation of the dynamic properties.

3.7.2.3 Parrinello-Rahman Barostat[76]

This method is very similar to the Andersen method but it allows the shape of the cell to change during the simulation. In this method two extra degrees of freedom are defined for the system: the kinetic energy of the system depends on a user-defined mass, W and the elastic energy term $p\Omega$. The difference between the internal stress and target pressure in the wall is the driving force for the shape change of the cell. This method can be used for the stress-strain relation studies since the shape of the cell is allowed to change.

3.8 Equilibration

Characterizing equilibrium is by no means an easy task, especially for small systems whose properties fluctuate considerably. Averaging over a series of timesteps will reduce the fluctuations, but different quantities relax to their equilibrium averages at different rates, and this must also be taken into account when trying to establish measurements.

Fortunately, relaxation is generally quite rapid, but one must always beware of those situations where this is not true specially for polymeric systems. Equilibration can be accelerated by starting the simulation at a higher temperature and later cooling by rescaling the velocities (this is similar, but not identical, to using a larger timestep initially); too high a temperature will, however, lead to numerical instability.

3.9 Periodic Boundary Conditions (PBC)

Periodic boundary conditions are used in systems where it is possible to neglect surface effects. These boundary conditions are implemented by performing the simulation in a small box and consider the physical system as replications of this simulation box in three dimensions. In simulations of planar surfaces, it is often useful to simulate two dimensions with periodic boundary conditions and use a different boundary condition in the third wall.

The main idea when using periodic boundary conditions is that the particle that exits the simulation cell from one surface enters the opposite surface with the same velocity. Only trajectories of the particles in the simulation box are stored.

Implementation of the periodic boundary condition in some special systems might be difficult. For instance in the simulations including waves, the wavelength is limited by the dimensions of the simulation cell. Or in the case of ionic systems, the net charge of the cell must be zero to avoid extreme charge accumulations. In spite of these limitations, periodic boundary conditions are often used for MD simulations of polymer systems.

Chapter 4

Results and Discussion

It was mentioned in Chapter 1 that aligned and continuous phases of the acceptor and donor materials are favorable to gain high efficiencies in polymer solar cells. Using diblock copolymers with acceptor and donor blocks is the newest approach to attain the desired nanomorphology in the active layer. Block copolymers are macromolecules composed of sequences or blocks of chemically distinct repeat units.[77] Upon blending of two thermodynamically incompatible homopolymers, they tend to form macroscopic domains of pure polymers. However, in the case of block copolymers, because of the covalent bond between separate blocks, they cannot separate to form macrodomains. Sizes of block copolymer domains depend on the polymerization number of the blocks. Diblock copolymers in the active layer, due to their tendency to self-segregate, do not need extra processing steps to attain a suitable nanomorphology and therefore are promising candidates for future PSCs.

A two-step process is usually followed to design new materials for PSCs. Firstly, an acceptor–donor pair must be designed which has the suitable optoelectronic properties. The second step is to synthesize the suggested materials and fabricate a solar cell to evaluate the morphology and efficiency attained using new materials. New material synthesis and characterization is very cumbersome and requires considerable amount of time, knowledge and budget. Moreover, due to the sensitivity of polymer solar cells to ambient, duration of light exposure, contact electrode degradation and processing conditions, the fabrication and performance evaluation of optimized solar cells is a delicate and multi-disciplinary process.

Failures to gain a high efficiency in newly-designed solar cells are mainly due to a poor nanomorphology in the active layer. Finding a computational method to evaluate the nanomorphology of the active layer can save a tremendous amount of time and investment. In the current work, we present a molecular dynamics (MD) method to predict the nanomorphology of the block copolymers commonly used in the PSCs.

The nanomorphology of a diblock copolymer, as mentioned in Chapter 2, depends on three factors: the A-B segment-segment Flory-Huggins interaction parameter (χ), the volume fraction of constituent blocks in the polymer (φ_A and φ_B) and the overall degree of polymerization (N). Volume fraction of blocks and the overall degree of polymerization can be readily controlled while synthesizing the block copolymer, the most important factor which determines nanostructure and degree of self-segregation is the Flory-Huggins interaction parameter. Finding suitable A and B blocks which have the proper χ parameter value and proper optoelectronic properties is the most important step in the design of a copolymer that will form the desired nanomorphology and hence will yield a higher power conversion efficiency. In the current chapter, Molecular Dynamics simulations are used to predict the nanomorphology of two block copolymers.

4.1 Molecular Dynamics Simulations

4.1.1 Simulation Parameters

All MD simulations were performed using the Materials Studio software package. (MS Modeling version 4.0, Accelrys)

The COMPASS force field[78] was used throughout the work to describe bonded and nonbonded interactions. In this forcefield:

$$E = E_b + E_\theta + E_\varphi + E_\chi + E_{nonbond} + E_{cross\text{-}coupling} \qquad 4.1$$

The first four terms represent bonded interactions that correspond to the energy associated with bond stretching (E_b), bond angle bending (E_θ), torsion angle rotations ($E\varphi$), and Wilson out-of-plane angle (E_χ). The nonbond term represents interactions consisting of Lennard-Jones (LJ) 9-6 function for the van der Waals interactions and the Coulombic function for the electrostatic interactions. Nonbond term is used for interactions between pairs of atoms that are separated by two or more intervening atoms or those that belong to different molecules. The cross-coupling term is used for the prediction of vibration frequencies and structural variations associated with conformational changes.

On the basis of first principle quantum mechanical calculations, the partial atomic charges on the molecules were preset by the COMPASS force field. The electrostatic interaction was calculated using the Ewald summation method because it provides a more effective way of handling long-range interactions.[79]

The amorphous cell which is constructed using Amorphous Cell module is usually in a high energy state so the Minimizer tool in the Discover module was used to minimize the energy of the systems and to remove Van der Waals overlaps. The Smart Minimization was used in this work which started with the steepest descent method, followed by the conjugate gradient method and ended with a Newton method. Velocities of atoms for the initial trajectory of each simulation are generated randomly using a Boltzmann distribution.

NPT simulations were used to compress the cell to its equilibrium volume to obtain its density. In these simulations, number of molecules in the cell, pressure and temperature were kept constant while volume of the cell changed. All NPT simulations were carried out at atmospheric pressure (0.0001 *GPa*). NPT simulations ought to be carried out until the density of the system is stabilized. In the case of NPT simulations, there is not a module to monitor the density of the system during the run so NPT simulations were performed in several intervals and the average density was evaluated after each interval. These runs were continued until the difference between the densities in consecutive steps was less than 0.4%. Simulation time for NPT runs are reported in Table 4.1. Berendsen thermostat and barostat[4] were used to keep temperature and pressure constant.

NVT simulations were used to calculate the potential energy of the system. In these simulations, the number of molecules in the cell, volume and temperature are kept constant. NPT ensemble was not used to calculate potential energy due to two reasons: firstly based on the lattice theory, the volume of the simulation cell must be kept constant. And higher computational speed is the second reason. In NVT ensemble, temperature is the only controllable variable but both pressure and temperature must be controlled in NPT ensembles. Berendsen thermostat[80] was used to keep temperature constant. The cell volume was calculated using the equilibrium density obtained from NPT simulations at the same temperature. NVT simulations were carried out until the potential energy of the system was stabilized. Simulation time for NVT runs are reported in Table 4.1.

Velocity Verlet[81] integrator is used to solve Newtonian equations of motion with a 1 *fs* timestep. The cutoff radius for Van der Waals interactions is 9.5 *Å* with 1 *Å* spline width.

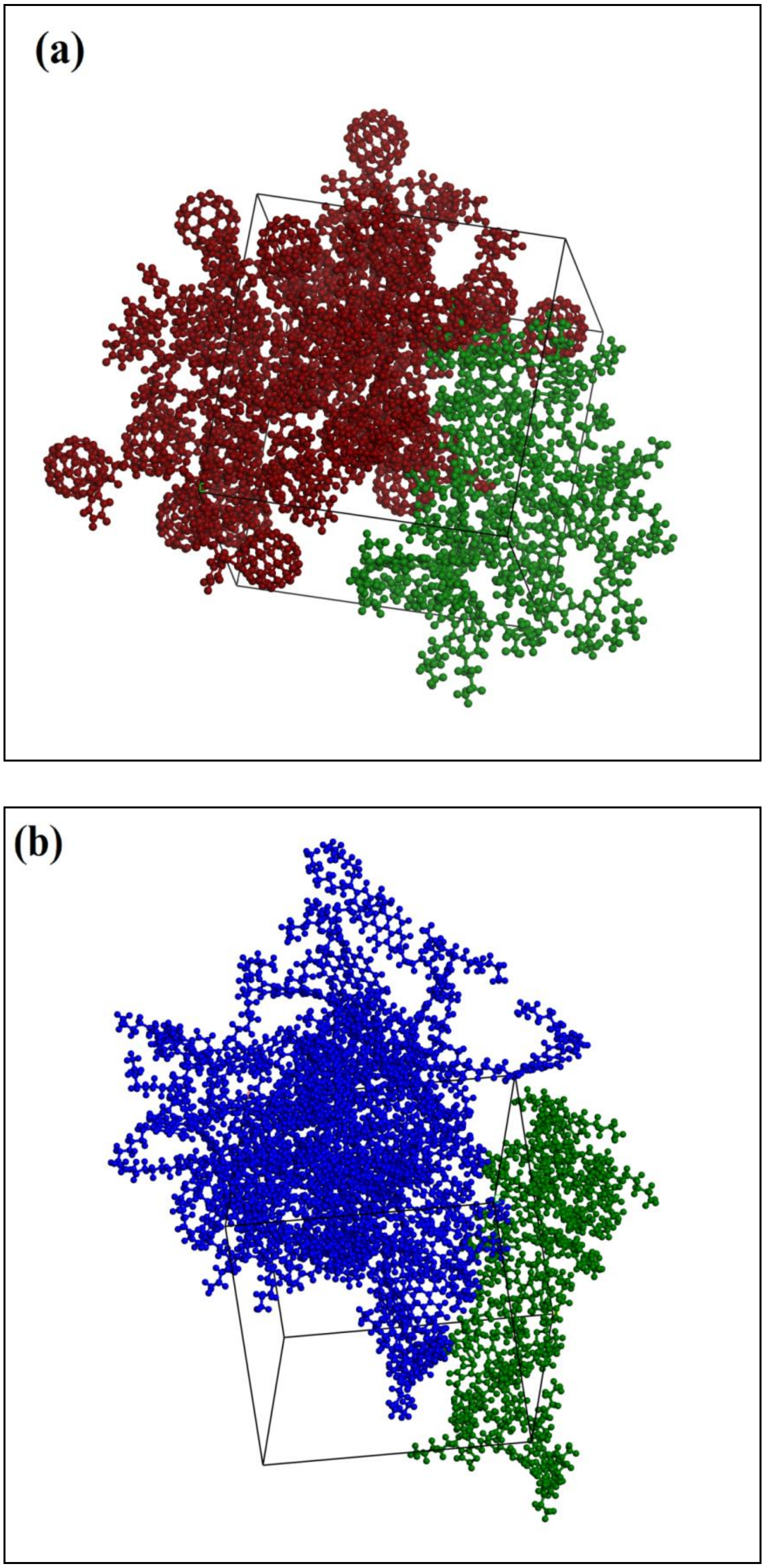

Figure 4.1: Amorphous cells of (a) P3HT and Poly(S_8A_2)-C_{60} blend with d = 1.173 g/cc, (b) P3HT and PPerAcr blend with d = 1.020 g/cc

4.1.2 Model Materials

P3HT is the acronym of poly(3-hexylthiophene), whose regioregular form[82] is used in solar cells owing to its superior optoelectronic properties. P3HT has been used as the donor material in BHJ solar cells extensively in recent years.[83-86] P3HT is the donor block in both systems that have been studied in the current work.

C_{60} in the form of PCBM has been used extensively in the past decade as the acceptor material. Several attempts have been made to synthesize C_{60}-containing blocks to be used in the polymer solar cells.[87-90] One example which is used in our work is Poly(S_xA_y)-C_{60} in which S stands for styrene and A stands for acrylate. Yang et al.[91] fabricated diblock copolymers with different x to y ratios and Poly(S_8A_2)-C_{60} yielded the best performance - hence it is used in the current work as the acceptor block. Figure 4.2 is the schematic representation of P3HT and Poly(S_8A_2)-C_{60} repeat units and P3HT-b-Poly(S_xA_y)-C_{60}.

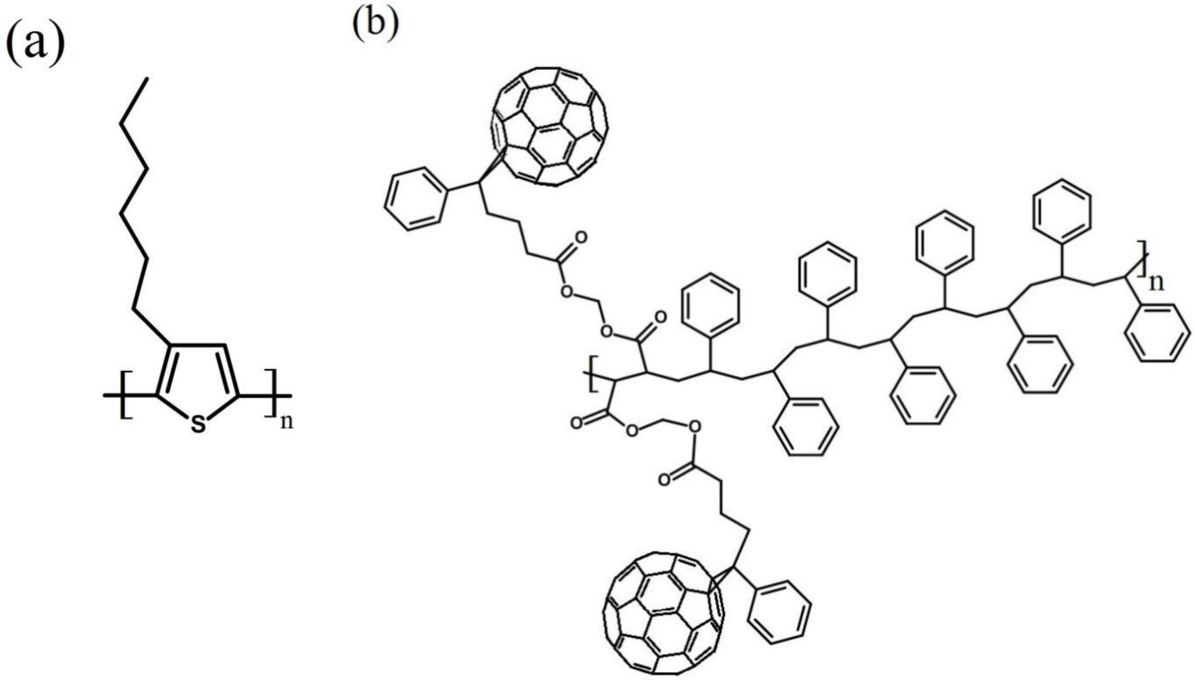

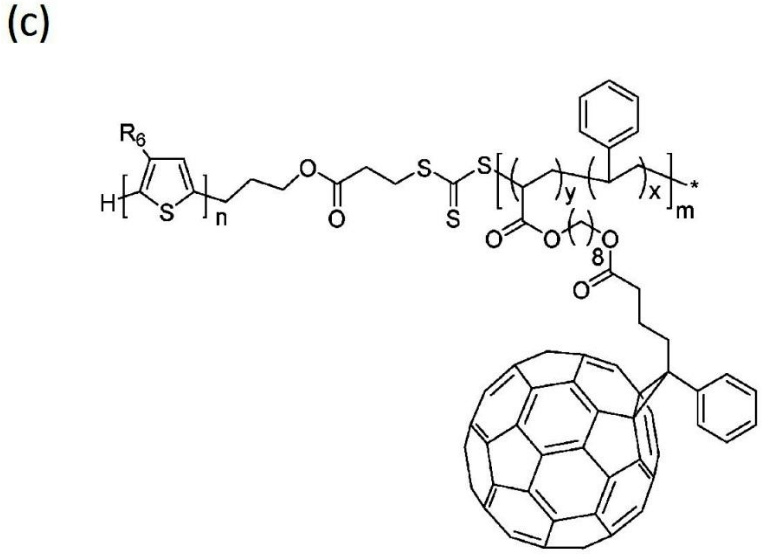

Figure 4.2: (a) P3HT repeat unit (3-hexylthiophene), (b) Poly(S_8A_2)-C_{60} repeat unit and (c) P3HT-b-Poly(S_xA_y)-C_{60}.

P3HT molecule with 40 (3-hexylthiophene) units for which MW = 8316.12 gr/mol and Poly(S_8A_2)-C_{60} with 10 repeat units for which MW = 29916.9 gr/mol are used in the simulations.

Electron transporting small molecules such as derivatives of perylene tetracarboxydiimide (PDI) have been used in PSCs as the acceptor materials. These molecules have the advantage of enhanced light absorption in the visible range but solar cells fabricated using these molecules tend to have a very low efficiency[92] due to the formation of micro-sized PDI crystals. Diblock copolymer fabrication is the best approach to prevent PDI crystal formation. Rajaram et al.[93] fabricated P3HT-b-Poly(n-butyl acrylate-*stat*-acrylate perylene) to address this topic. This copolymer is used for our simulations.

PPerAcr with 40 repeat units for which MW = 33006.1 gr/mol is used for simulations.

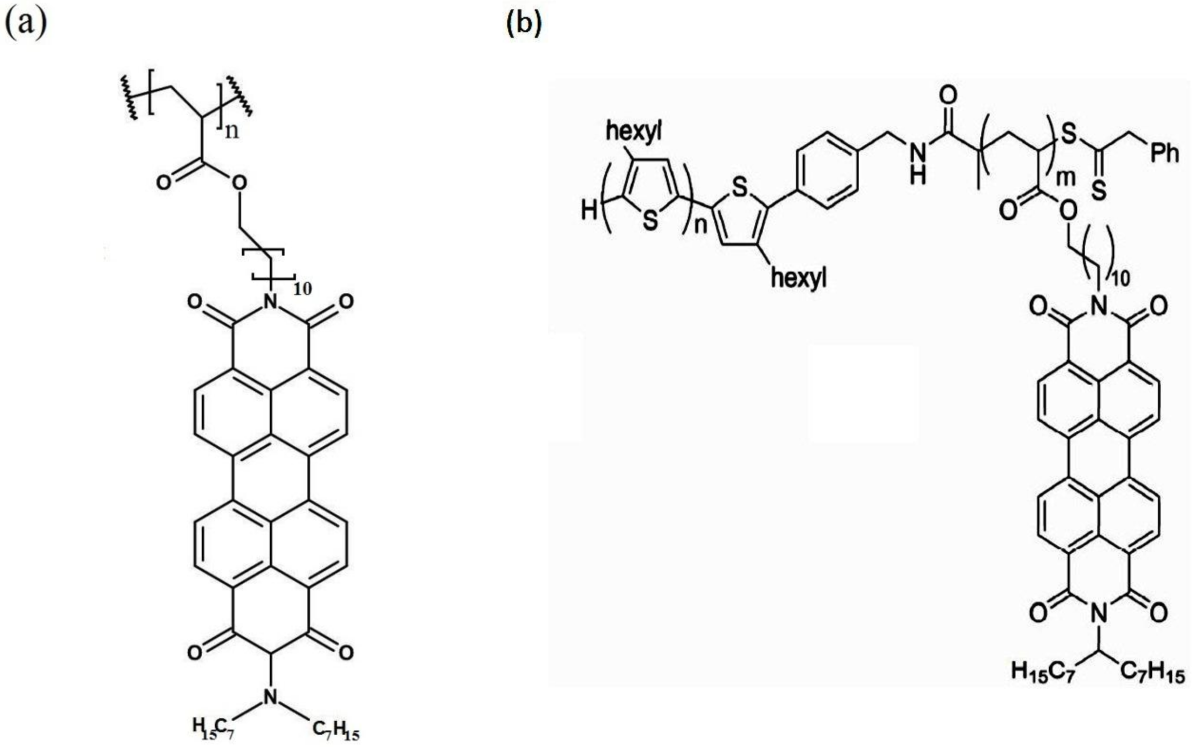

Figure 4.3: (a) PPerAcr repeat unit and (b) P3HT-b-Poly(n-butyl acrylate-stat-acrylate perylene).

4.1.3 Simulation Results

Table 4.1 shows the computed density values of the pure components of the blocks that make up of the diblock copolymers of interest and their binary blends after NPT MD annealings.

Table 4.1: NPT Molecular Dynamics Simulation Results

	T (K)	Density (g/cc)	NPT Simulation time (*ps*)	NVT simulation time (*ps*)
P3HT	500	0.973	2800	1000
	550	0.943	2800	1000
	600	0.921	1900	800
	650	0.891	1600	600

Table 4.1, Continued

PPerAcr	500	1.046	80	240
	550	1.040	80	120
	600	1.017	60	120
	650	1.004	60	80
P3HT and PPerAcr Blend	500	1.020	160	120
	550	1.001	160	80
	600	0.985	160	70
	650	0.967	120	40
Poly(S_8A_2)-C_{60}	500	1.291	450	300
	550	1.275	450	300
	600	1.258	450	300
	650	1.245	450	300
P3HT and Poly(S_8A_2)-C_{60} blend	500	1.204	400	300
	550	1.190	400	300
	600	1.173	400	300
	650	1.161	400	300

Volume fractions of blocks in the diblock copolymer were then calculated using the density values of the pure blocks and of their molar weight using Equation 4.2:

$$\varphi_1 = \frac{V_1}{V_t} = \frac{\frac{m_1}{\rho_1}}{V_t} = \frac{\frac{n_1 MW_1}{\rho_1}}{\frac{n_1 MW_1}{\rho_1} + \frac{n_2 MW_2}{\rho_2}} \qquad 4.2$$

where n_1 and n_2 are the number of polymer molecules in the simulation box and ρ_i is the polymer density.

And the Flory-Huggins interaction parameter was calculated using Equation 4.3.

$$\chi = \frac{\Delta E_{mix}}{N_t kT \varphi_A \varphi_B} \qquad 4.3$$

ΔE_{mix} (mixing potential energy) is the difference between the potential energy of binary blends and the corresponding pure homopolymers:

$$\Delta E_{mix} = E_{blend} - E_1 - E_2 \qquad 4.4$$

The results of such calculations are summarized in Table 4.2.

Table 4.2: Polymer-polymer χ parameters

	T (K)	P3HT Volume Fraction	ΔE_{mix} (kcal/mol)	Polymer-Polymer χ parameter
P3HT-b-PPerAcr	500	0.2133	53	322
	550	0.2175	43	236
	600	0.2176	37	183
	650	0.2210	18	81
P3HT-b-Poly(S_8A_2)-C_{60}	500	0.2696	1245	6366
	550	0.2732	1252	5771
	600	0.2751	1234	5193
	650	0.2801	1188	4561

The values listed in Table 4.2 are Polymer-Polymer χ parameters. However, in order to use diblock copolymer phase diagrams in the prediction of the nanomorphology, these values should be converted to the segment-segment χ parameter by dividing them by the total number of lattice sites in the simulation cell. Based on the lattice theory, the volume of each lattice site is considered to be equal to the smaller of segment volumes of the components involved. The total number of sites in the simulation cell can be obtained by dividing the total cell volume by the volume of a P3HT segment. The total cell volume is obtained from Equation 4.5:

$$V_{cell} = \frac{MW_1 + MW_2}{\rho_{blend}} \qquad 4.5$$

The results are shown in Table 4.3.

Table 4.3: Calculated the segment-segment χ parameters

	T (K)	Total Cell Volume ($cc/mol_{copolymer}$)	Lattice Site Number	Segment-Segment χ parameter
P3HT-b-PPerAcr	500	40504	236.8	1.36
	550	41260	233.9	1.01

	600	41960	232.5	0.79
	650	42746	229.1	0.35
P3HT-b-Poly(S_8A_2)-C_{60}	500	31766	185.7	34.27
	550	32118	182.1	31.69
	600	32607	180.7	28.75
	650	32942	176.5	25.84

Flory-Huggins interaction parameter decreases with temperature increase and in most of the cases, there is linear correlation between χ-value and reciprocal temperature:

$$\chi \approx \alpha T^{-1} + \beta, \alpha > 0 \tag{4.6}$$

It is obvious that the temperature dependence of the segment-segment χ parameters reported in table 4.3 exhibits the same trend as predicted by Equation 4.6 (see Figures 4.4 and 4.5) for both systems, indicating that the pure components would phase segregate at low temperatures.

The question here is whether the computed the segment-segment χ parameters predict the nanomorphology of the diblock copolymers. To evaluate the effectiveness of MD simulations as a prognostication tool, a comparison will be made between predictions of the MD simulation results along the use of the block copolymer theory and AFM images of experimental works. Results of Yang et al.[91] for P3HT-b-Poly(S_8A_2)-C_{60} and results of Tao et al.[94] for P3HT-b-PTP4AP are used in these comparisons.

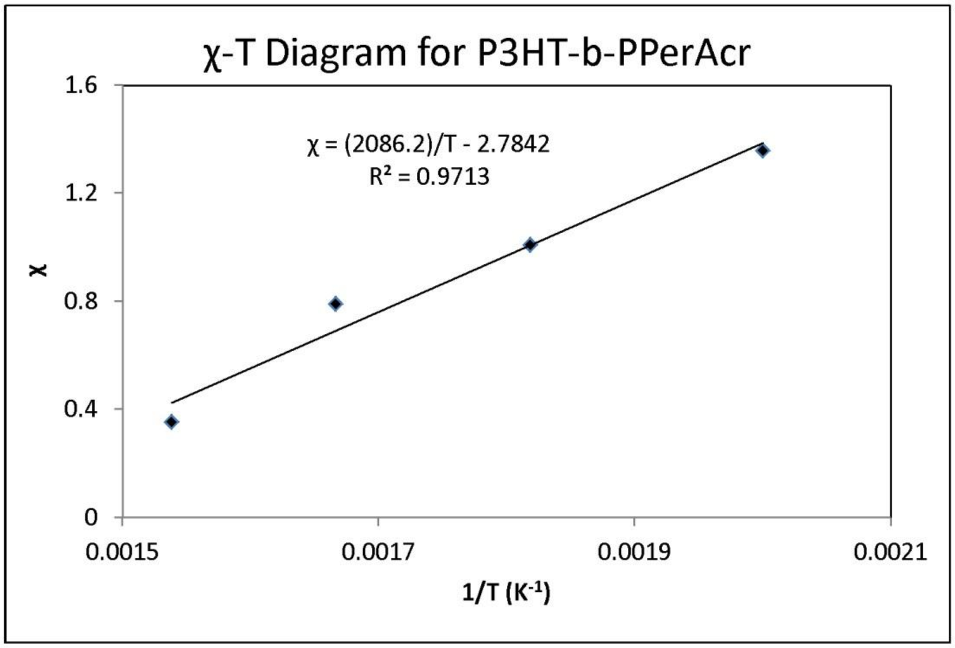

Figure 4.4: Temperature dependence of χ for P3HT-b-PPerAcr

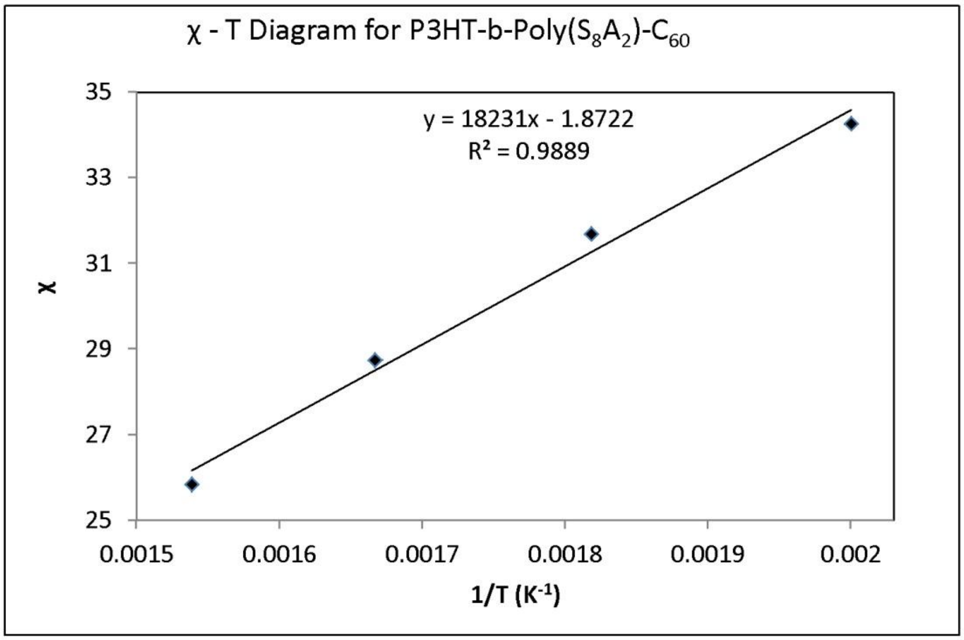

Figure 4.5: Temperature dependence of χ for P3HT-b-Poly(S_8A_2)-C_{60}

To predict the phase nanomorphology, the total degrees of polymerization (*N*) of the diblock copolymers used in the computational studies and volume fraction of each block are needed in addition to the χ parameter. Data provided by Yang et al.[91] is summarized in Table 4.4.

Table 4.4: Experimental data provided for P3HT-b-Poly(S8A2)-C60 by Yang et al.[15]

3-hexylthiophene mol%	Styrene mol%	Acrylate mol%	MW (g/mol)
12	71	17	18,500

Based on these data the following information can be obtained for P3HT-b-Poly(S_8A_2)-C_{60}:

Table 4.5: The total degree of polymerization and volume fractions of the blocks of system 1

Degree of polymerization	13.67
φ_{P3HT}	0.094
$\varphi_{P(S8A2)\text{-}C60}$	0.906
χN in 600 K	393

Based on the values shown in Table 4.5, pure P3HT cylinders inside Poly(S_8A_2)-C_{60} phase are expected. AFM image of the P3HT-b-Poly(S_8A_2)-C_{60} phase published by Yang et al.[91] shows formation of P3HT cylindrical boundaries which is consistent with our prediction.

For P3HT-b-PPerAcr copolymer, χ values are much smaller than those of P3HT-b-Poly(S_8A_2)-C_{60} so it is expected that it will not form completely pure phases with sharp interface but its χ values are large enough to be in the intermediate segregation limit. AFM image of P3HT-b-PTP4AP (Tao et al.[94]), a diblock copolymer (see Figure 4.6) with acrylate as the acceptor block but similar to the one we used in the present work, shows a phase separation occurrence with a lower degree in comparison with P3HT-b-Poly(S_8A_2)-C_{60} case.

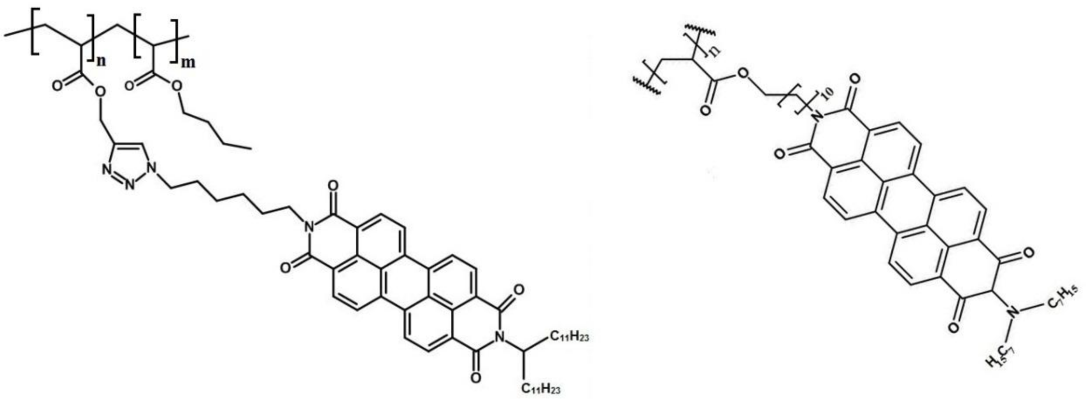

PTP4AP **PPerAcr**

Figure 4.6: Schematic comparison of PTP4AP and PPerAcr

4.2 Pair Distribution Functions

Pair Distribution Function describes the distribution of distances between pairs of particles in a given volume. The function which is usually denoted by g(r) is the probability of finding a particle at the distance *r* from the denoted particle. Pair distribution function can provide another tool to validate phase segregation in block copolymers. Figure 4.7 shows pair distribution functions for hydrogen atoms of P3HT molecule for three cases: pure P3HT, P3HT-PPerAcr mixture and P3HT-Poly(S_8A_2)-C_{60} mixture. In the case of the pure P3HT the intermolecular contribution becomes greater than the intramolecular contribution at distances farther than 5Å from the designated atom while in the case of the blends, the intramolecular contribution is superior throughout the domain. This proves that in the case of blends, there is a barrier of PPerAcr or Poly(S_8A_2)-C_{60} molecules between P3HT molecules.

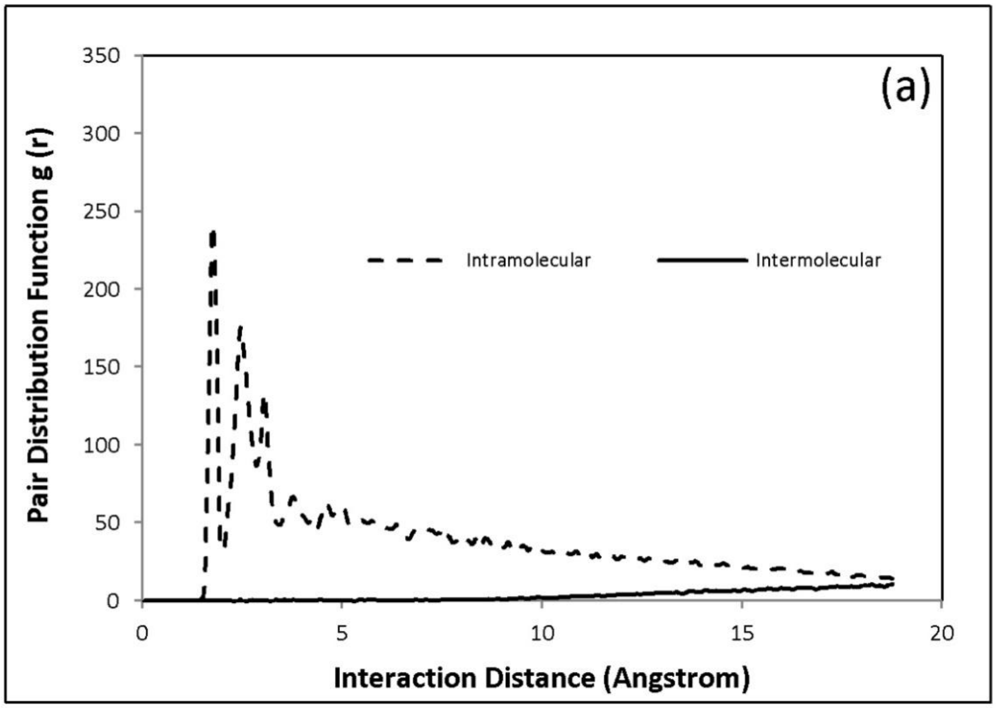
350
300
250
200
150
100
50
0
Pair Distribution Function g (r)
(a)
Intramolecular
Intermolecular
0
5
10
15
20
Interaction Distance (Angstrom)

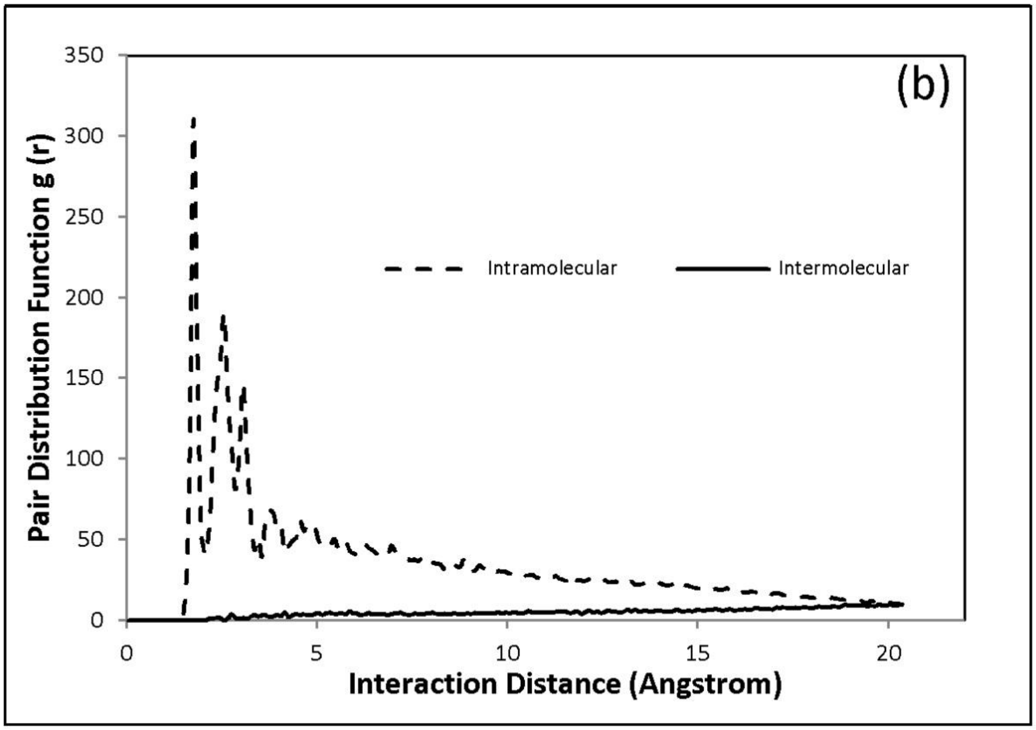
350
300
250
200
150
100
50
0
Pair Distribution Function g (r)
(b)
Intramolecular
Intermolecular
0
5
10
15
20
Interaction Distance (Angstrom)

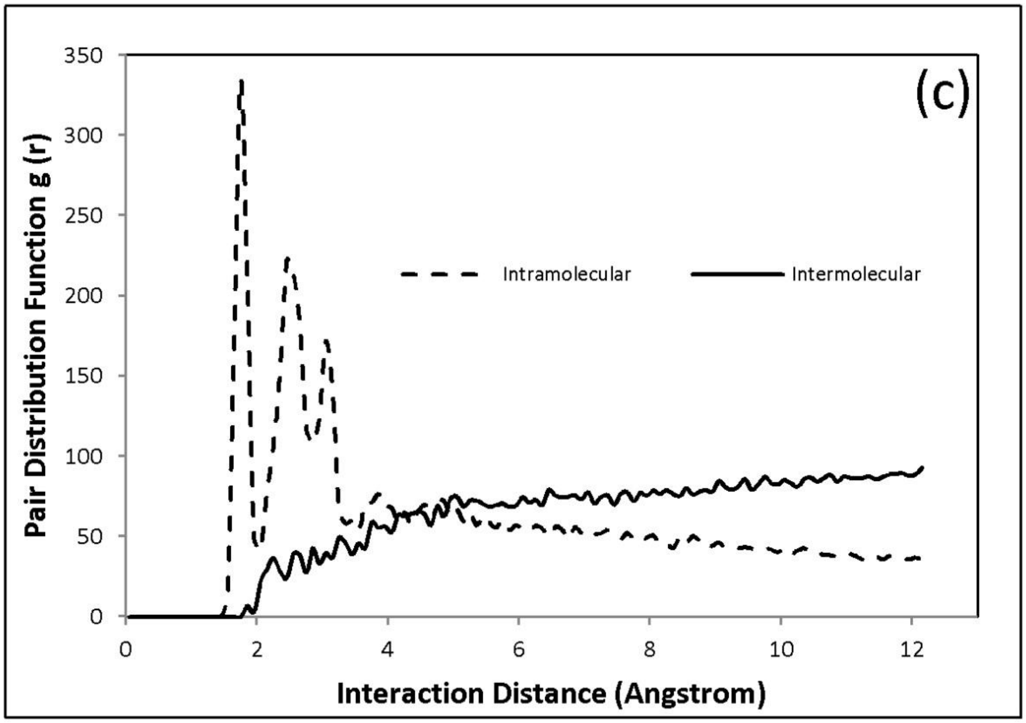

Figure 4.7: Pair Distribution function plots for hydrogen atoms of P3HT in (a) P3HT and Poly(S_8A_2)-C_{60} blend, (b) P3HT and PPerAcr blend, (c) Pure P3HT.

Based upon the above results, we expect that the MD approach can be used to predict the nanomorphology of diblock copolymers used in the active layer of PSCs.

Chapter 5

Conclusion

As mentioned in chapter 1, the ideal architecture for high efficiency solar cells consists of an ordered bulk heterojunction with charge percolation pathways for both types of charge carriers and separated donor and acceptor phases of size comparable to their respective exciton diffusion lengths. In pursuit of this goal, hybrid solar cells consisting of inorganic n-type large band-gap ZnO or TiO_2 nanorod/nanotube arrays filled with a p-type semiconducting polymer have attracted much interest. In contrast, all-organic ordered heterojunctions could have simpler processing and can also be designed to absorb light more efficiently by incorporating n-type absorber. However, all-organic ordered heterojunction solar cells have presently not been achieved due to material compatibility issues. For instance, when it is attempted to fill nanorod arrays of a acceptor with a corresponding solution processed donor (or vice-versa), the nanorod array architecture softens, buckles, recrystallizes or otherwise changes its morphology due to the effect of the organic solvent(s) used in the subsequent step. The use of diblock copolymers that vertically phase segregate into cylindrical domains offers a solution to this vexing problem, and allows the construction of ordered heterojunction solar cells. Our work advances the systematic design of such diblock copolymers, and highlights the predictive value of molecular dynamics simulations in pre-testing the morphology of such diblock copolymer films.

Bibliography

[1] Kamat, P. V. 2007. Meeting the clean energy demand: Nanostructure architectures for solar energy conversion. *Journal of Physical Chemistry C* 111 (7): 2834-60.

[2] Lewis, N. S. 2007. Toward cost-effective solar energy use. *Science* 315 (5813): 798-801.

[3] Li, G., V. Shrotriya, J. S. Huang, Y. Yao, T. Moriarty, K. Emery, and Y. Yang. 2005. High-efficiency solution processable polymer photovoltaic cells by self-organization of polymer blends. *Nature Materials* 4 (11) (NOV): 864-8.

[4] http://www.solarmer.com/productbipv.php evaluated on March 28, 2011

[5] Po, R., C. Carbonera, A. Bernardi, and N. Camaioni. 2011. The role of buffer layers in polymer solar cells. *Energy and Environmental Science* 4 (2): 285-310.

[6] http://www.heliatek.com/

[7] http://www.konarka.com/

[8] http://www.solarmer.com/

[9] Tvingstedt, K.; Vandewal, K.; Zhang, F. L.; Inganas, O., On the Dissociation Efficiency of Charge Transfer Excitons and Frenkel Excitons in Organic Solar Cells: A Luminescence Quenching Study. *Journal of Physical Chemistry C* **2010,** *114* (49), 21824-21832.

[10] Lunt, R. R.; Benziger, J. B.; Forrest, S. R., Relationship between Crystalline Order and Exciton Diffusion Length in Molecular Organic Semiconductors. *Advanced Materials* **2010,** *22* (11), 1233-1236.

[11] Markov, D. E.; Amsterdam, E.; Blom, P. W. M.; Sieval, A. B.; Hummelen, J. C., Accurate Measurement of the Exciton Diffusion Length in a Conjugated Polymer Using a Heterostructure with a Side-Chain Cross-Linked Fullerene Layer. *The Journal of Physical Chemistry A* **2005,** *109* (24), 5266-5274.

[12] Coakley, K. M., and M. D. McGehee. 2004. Conjugated polymer photovoltaic cells. *Chemistry of Materials* 16 (23) (NOV 16): 4533-42.

[13] Chen, F.C, J.L Wu, S. S. Yang, K.H Hsieh, and W.C Chen. 2008. Cesium carbonate as a functional interlayer for polymer photovoltaic devices. *Journal of Applied Physics* 103 (10).

[14] Yang, F., M. Shtein, and S. R. Forrest. 2005. Controlled growth of a molecular bulk heterojunction photovoltaic cell. *Nature Materials* 4 (1) (JAN): 37-41.

[15] Bundgaard, E., O. Hagemann, M. Manceau, M. Jørgensen, and F. C. Krebs. 2010. Low band gap polymers for roll-to-roll coated polymer solar cells. *Macromolecules* 43 (19): 8115-20.

[16] Peet, J., J. Y. Kim, N. E. Coates, W. L. Ma, D. Moses, A. J. Heeger, and G. C. Bazan. 2007. Efficiency enhancement in low-bandgap polymer solar cells by processing with alkane dithiols. *Nature Materials* 6 (7): 497-500.

[17] Helgesen, M., R. Søndergaard, and F. C. Krebs. 2010. Advanced materials and processes for polymer solar cell devices. *Journal of Materials Chemistry* 20 (1): 36-60.

[18] Ma, W. L., C. Y. Yang, X. Gong, K. Lee, and A. J. Heeger. 2005. Thermally stable, efficient polymer solar cells with nanoscale control of the interpenetrating network morphology. *Advanced Functional Materials* 15 (10) (OCT): 1617-22.

[19] Vanlaeke, P., A. Swinnen, I. Haeldermans, G. Vanhoyland, T. Aernouts, D. Cheyns, C. Deibel, et al. 2006. P3HT/PCBM bulk heterojunction solar cells: Relation between morphology and electro-optical characteristics. *Solar Energy Materials and Solar Cells* 90 (14) (SEP 6): 2150-8.

[20] Swinnen, A., I. Haeldermans, M. Vande Ven, J. D'Haen, G. Vanhoyland, S. Aresu, M. D'Olieslaeger, and J. Manca. 2006. Tuning the dimensions of C60-based needlelike crystals in blended thin films. *Advanced Functional Materials* 16 (6): 760-5.

[21] Bechara, R., N. Leclerc, P. Ĺv̂que, F. Richard, T. Heiser, and G. Hadziioannou. 2008. Efficiency enhancement of polymer photovoltaic devices using thieno-thiophene based copolymers as nucleating agents for polythiophene crystallization. *Applied Physics Letters* 93 (1).

[22] Po, R., M. Maggini, and N. Camaioni. 2010. Polymer solar cells: Recent approaches and achievements. *Journal of Physical Chemistry C* 114 (2): 695-706.

[23] Roman, L. S., Mammo, W., Pettersson, L. A. A., Andersson, M. R., & Inganäs, O. (1998). High quantum efficiency polythiophene/C60 photodiodes. *Advanced Materials, 10*(10), 774-777.

[24] Chapter 7 in Organic Photovoltaics: Materials, Device Physics, and Manufacturing Technologies, ed. C. J. Brabec, V. Dyakonov and U. Scherf, *Wiley VCH Verlag GmbH & Co*. KGaA, Weinheim, 2008.

[25] Nguyen, T. P., & De Vos, S. A. (2004). An investigation into the effect of chemical and thermal treatments on the structural changes of poly(3,4-ethylenedioxythiophene)/polystyrenesulfonate and consequences on its use on indium tin oxide substrates. *Applied Surface Science, 221*(1-4), 330-339.

[26] Koch, N., Vollmer, A., & Elschner, A. (2007). Influence of water on the work function of conducting poly(3,4-ethylenedioxythiophene)/poly(styrenesulfonate).*Applied Physics Letters, 90*(4)

[27] Brabec, C. J., S. E. Shaheen, C. Winder, N. Serdar Sariciftci, and P. Denk. 2002. Effect of LiF/metal electrodes on the performance of plastic solar cells. *Applied Physics Letters* 80 (7): 1288.

[28] Jiang, X., H. Xu, L. Yang, M. Shi, M. Wang, and H. Chen. 2009. Effect of CsF interlayer on the performance of polymer bulk heterojunction solar cells. *Solar Energy Materials and Solar Cells* 93 (5): 650-3.

[29] Chen, F. -C, J. -L Wu, S. S. Yang, K. -H Hsieh, and W. -C Chen. 2008. Cesium carbonate as a functional interlayer for polymer photovoltaic devices. *Journal of Applied Physics* 103 (10).

[30] Kim, J. Y., S. H. Kim, H. -H Lee, K. Lee, W. Ma, X. Gong, and A. J. Heeger. 2006. New architecture for high-efficiency polymer photovoltaic cells using solution-based titanium oxide as an optical spacer. *Advanced Materials* 18 (5): 572-6.

[31] White, M. S., D. C. Olson, S. E. Shaheen, N. Kopidakis, and D. S. Ginley. 2006. Inverted bulk-heterojunction organic photovoltaic device using a solution-derived ZnO underlayer. *Applied Physics Letters* 89 (14).

[32] Hau, S. K., H. -L Yip, and A. K. -Y Jen. 2010. A review on the development of the inverted polymer solar cell architecture. *Polymer Reviews* 50 (4): 474-510.

[33] Zhang, F., X. Xu, W. Tang, J. Zhang, Z. Zhuo, J. Wang, J. Wang, Z. Xu, and Y. Wang. Recent development of the inverted configuration organic solar cells. *Solar Energy Materials and Solar Cells*.

[34] Hiramoto, M., M. Suezaki, and M. Yokoyama. 1990. Effect of thin gold interstitial-layer on the photovoltaic properties of tandem organic solar-cell. *Chemistry Letters*(3) (MAR): 327-30.

[35] Yakimov, A., and S. R. Forrest. 2002. High photovoltage multiple-heterojunction organic solar cells incorporating interfacial metallic nanoclusters. *Applied Physics Letters* 80 (9): 1667.

[36] Uchida, S., J. Xue, B. P. Rand, and S. R. Forrest. 2004. Organic small molecule solar cells with a homogeneously mixed copper phthalocyanine: C60 active layer. *Applied Physics Letters* 84 (21): 4218-20.

[37] Xue, J., S. Uchida, B. P. Rand, and S. R. Forrest. 2004. Asymmetric tandem organic photovoltaic cells with hybrid planar-mixed molecular heterojunctions. *Applied Physics Letters* 85 (23): 5757-9.

[38] Dennler, G., H. -J Prall, R. Koeppe, M. Egginger, R. Autengruber, and N. S. Sariciftci. 2006. Enhanced spectral coverage in tandem organic solar cells. *Applied Physics Letters* 89 (7).

[39] Shrotriya, V., E. H. -E Wu, G. Li, Y. Yao, and Y. Yang. 2006. Efficient light harvesting in multiple-device stacked structure for polymer solar cells. *Applied Physics Letters* 88 (6).

[40] Kawano, K., N. Ito, T. Nishimori, and J. Sakai. 2006. Open circuit voltage of stacked bulk heterojunction organic solar cells. *Applied Physics Letters* 88 (7).

[41] Gilot, J., M. M. Wienk, and R. A. J. Janssen. 2007. Double and triple junction polymer solar cells processed from solution. *Applied Physics Letters* 90 (14).

[42] Jin, Y. K., K. Lee, N. E. Coates, D. Moses, T. -Q Nguyen, M. Dante, and A. J. Heeger. 2007. Efficient tandem polymer solar cells fabricated by all-solution processing. *Science* 317 (5835): 222-5.

[43] Krebs, F. C. 2009. Fabrication and processing of polymer solar cells: A review of printing and coating techniques. *Solar Energy Materials and Solar Cells* 93 (4): 394-412.

[44] Espinosa, N., R. García-Valverde, A. Urbina, and F. C. Krebs. 2011. A life cycle analysis of polymer solar cell modules prepared using roll-to-roll methods under ambient conditions. *Solar Energy Materials and Solar Cells* 95 (5): 1293-302.

[45] http://www.heliatek.com/ evaluated on March 04, 2011

[46] European Photovoltaic Industry Association (EPIA). 2011. Solar generation 6, Solar photovoltaic electricity empowering the world. Online at: http://www.greenpeace.org/international/Global/international/publications/climate/2010/SolarGeneration2010.pdf

[47] Jørgensen, M., K. Norrman, and F. C. Krebs. 2008. Stability/degradation of polymer solar cells. *Solar Energy Materials and Solar Cells* 92 (7): 686-714.

[48] Hildebrand JH. A Quantitative Treatment of Deviations from Raoult's Law. Proc Natl Acad Sci U S A. 1927 May;13(5):267–272.

[49] Flory, P.J. Principles *of polymer chemistry,* Cornell University Press: New York (1953)

[50] KRAUSE, S. (1969). Microphase separation in block copolymers - zeroth approximation. *Journal of Polymer Science Part A-2-Polymer Physics, 7*(1PA2), 249-&.

[51] KRAUSE, S. (1970). Microphase separation in block copolymers . zeroth approximation including surface free energies. *Macromolecules, 3*(1), 84-&.

[52] Krause, S., Dunn, D. J., Seyedmozzaffari, A., & Biswas, A. M. (1977). Microphase separation in diblock and triblock copolymers of styrene and alpha-methylstyrene. *Macromolecules, 10*(4), 786-790.

[53] Krause, S., Dunn, D. J., Seyedmozzaffari, A., & Biswas, A. M. (1977). Microphase separation in diblock and triblock copolymers of styrene and alpha-methylstyrene. *Macromolecules, 10*(4), 786-790.

[54] MEIER, D. (1969). Theory of block copolymers .I. domain formation in A-B block *copolymers*. *Journal of Polymer Science Part C-Polymer Symposium,* (26PC), 81-&.

[55] Dunn, D. J., & Krause, S. (1974). Phase separation in diblock copolymers of styrene and alpha-methyl styrene and in mixtures of corresponding homopolymers. *Journal of Polymer Science Part C-Polymer Letters, 12*(10), 591-596.

[56] Fredrickson, G. H., and F. S. Bates. 1996. Dynamics of block copolymers: Theory and experiment. *Annual Review of Materials Science* 26 (1): 501-50.

[57] Olemskoi, A., and A. Savelyev. 2005. Theory of microphase separation in homopolymer-oligomer mixtures. *Physics Reports* 419 (4-5): 145-205.

[58] Rosedale, J. H., F. S. Bates, K. Almdal, K. Mortensen, and G. D. Wignall. 1995. Order and disorder in symmetric diblock copolymer melts. *Macromolecules* 28 (5): 1429-43.

[59] Bates, F. S., and G. H. Fredrickson. 1990. Block copolymer thermodynamics: Theory and experiment. *Annual Review of Physical Chemistry* 41 (1): 525-57.

[60] Fredrickson, G. H., & Helfand, E. (1987). Fluctuation effects in the theory of microphase separation in block copolymers. *The Journal of Chemical Physics, 87*(1), 697-705.

[61] Khandpur, A. K., S. Förster, F. S. Bates, I. W. Hamley, A. J. Ryan, W. Bras, K. Almdal, and K. Mortensen. 1995. Polyisoprene-polystyrene diblock copolymer phase diagram near the order-disorder transition. *Macromolecules* 28 (26): 8796-806.

[62] METROPOLIS, N., & ULAM, S. (1949). The monte carlo method. *Journal of the American Statistical Association, 44*(247), 335-341.

[63] Alder, B. J., & Wainwright, T. E. (1959). Studies in molecular dynamics. I. general method. *The Journal of Chemical Physics, 31*(2), 459-466.

[64] Flory, P. J. (1974). Foundations of rotational isomeric state theory and general methods for generating configurational averages. *Macromolecules, 7*(3), 381-392.

[65] Mattice, W. L.; Suter, U. W. Conformational Theory of Large Molecules: The Rotational Isomeric State Model in Macromolecular Systems; *J. Wiley*: New York, 1994.

[66] Flory, P.J. *Statistical Mechanics of Chain Molecules,* Interscience: New York (1969)

[67] Lewars, E. G. *Computational Chemistry. Introduction to the Theory and Applications of Molecular and Quantum Mechanics,* Kluwer Academic Publishers: New York, 2003.

[68] Infrared spectroscopy: R. M. Silverstein, G. C. Bassler and T. C. Morrill, “Spectrometric Identification of Organic Compounds,” 4th edn, Wiley, New York, 1981.

[69] Verlet, L. (1967). Computer "experiments" on classical fluids. I. Thermodynamical properties of Lennard-Jones molecules. *Physical Review, 159*(1), 98-103.

[70] Swope, W. C., Andersen, H. C., Berens, P. H., & Wilson, K. R. (1982). A computer simulation method for the calculation of equilibrium constants for the formation of physical clusters of molecules: Application to small water clusters. *The Journal of Chemical Physics, 76*(1), 637-649.

[71] Berendsen, H. J. C., Postma, J. P. M., Van Gunsteren, W. F., Dinola, A., & Haak, J. R. (1984). Molecular dynamics with coupling to an external bath. *The Journal of Chemical Physics, 81*(8), 3684-3690.

[72] Andersen, H. C. (1980). Molecular dynamics simulations at constant pressure and/or temperature. *The Journal of Chemical Physics, 72*(4), 2384-2393.

[73] Nosé, S. "A molecular dynamics method for simulations in the canonical ensemble", *Mol. Phys.*, **52**, 255-268 (1984).

[74] Nosé, S. "A unified formulation of the constant temperature molecular dynamics methods", *J. Chem. Phys.*, **81**, 511-519 (1984).

[75] Nosé, S. "Constant temperature molecular dynamics methods", *Prog. Theor. Phys., Suppl.*, **103**, 1-46 (1991).

[76] **Parrinello,** M., & Rahman, A. (1981). Polymorphic transitions in single crystals: A new molecular dynamics method. *Journal of Applied Physics, 52*(12), 7182-7190.

[77] Bates, F. S., and G. H. Fredrickson. 1990. Block copolymer thermodynamics: Theory and experiment. *Annual Review of Physical Chemistry* 41 (1): 525-57.

[78] Sun, H. 1998. Compass: An ab initio force-field optimized for condensed-phase applications - overview with details on alkane and benzene compounds. *Journal of Physical Chemistry B* 102 (38): 7338-64.

[79] Sagui, C., and Darden, T. A. *Molecular dynamics simulations of biomolecules: Long-range electrostatic effects.*1999.

[80] Berendsen, H. J. C., Postma, J. P. M., Van Gunsteren, W. F., Dinola, A., & Haak, J. R. (1984). Molecular dynamics with coupling to an external bath. *The Journal of Chemical Physics, 81*(8), 3684-3690.

[81] Swope, W. C., Andersen, H. C., Berens, P. H., & Wilson, K. R. (1982). A computer simulation method for the calculation of equilibrium constants for the formation of physical clusters of molecules: Application to small water clusters. *The Journal of Chemical Physics, 76*(1), 637-649.

[82] Kim, Y., S. Cook, S. M. Tuladhar, S. A. Choulis, J. Nelson, J. R. Durrant, D. D. C. Bradley, et al. 2006. A strong regioregularity effect in self-organizing conjugated polymer films and high-efficiency polythiophene:Fullerene solar cells. *Nature Materials* 5 (3): 197-203.

[83] Li, G., V. Shrotriya, J. S. Huang, Y. Yao, T. Moriarty, K. Emery, and Y. Yang. 2005. High-efficiency solution processable polymer photovoltaic cells by self-organization of polymer blends. *Nature Materials* 4 (11) (NOV): 864-8.

[84] Reyes-Reyes, M., K. Kim, and D. L. Carroll. 2005. High-efficiency photovoltaic devices based on annealed poly(3-hexylthiophene) and 1-(3-methoxycarbonyl)-propyl-1- phenyl- (6,6) C61 blends. *Applied Physics Letters* 87 (8): 1-3.

[85] Kim, Y., S. A. Choulis, J. Nelson, D. D. C. Bradley, S. Cook, and J. R. Durrant. 2005. Device annealing effect in organic solar cells with blends of regioregular poly(3-hexylthiophene) and soluble fullerene. *Applied Physics Letters* 86 (6): 1-3.

[86] Padinger, F., R. S. Rittberger, and N. S. Sariciftci. 2003. Effects of postproduction treatment on plastic solar cells. *Advanced Functional Materials* 13 (1): 85-8.

[87] Van Der Veen, M. H., B. De Boer, U. Stalmach, K. I. Van De Wetering, and G. Hadziioannou. 2004. Donor - acceptor diblock copolymers based on PPV and C60: Synthesis, thermal properties, and morphology. *Macromolecules* 37 (10): 3673-84.

[88] Stalmach, U., B. De Boer, C. Videlot, P. F. Van Hutten, and G. Hadziioannou. 2000. Semiconducting diblock copolymers synthesized by means of controlled radical polymerization techniques. *Journal of the American Chemical Society* 122 (23): 5464-72.

[89] Barrau, S., T. Heiser, F. Richard, C. Brochon, C. Ngov, K. Van De Wetering, G. Hadziioannou, D. V. Anokhin, and D. A. Ivanov. 2008. Self-assembling of novel fullerene-grafted donor-acceptor rod-coil block copolymers. *Macromolecules* 41 (7): 2701-10.

[90] De Boer, B., U. Stalmach, P. F. Van Hutten, C. Melzer, V. V. Krasnikov, and G. Hadziioannou. 2001. Supramolecular self-assembly and opto-electronic properties of semiconducting block copolymers. *Polymer* 42 (21): 9097-109.

[91] Yang, C., J. K. Lee, A. J. Heeger, and F. Wudl. 2009. Well-defined donor-acceptor rod-coil diblock copolymers based on P3HT containing C60: The morphology and role as a surfactant in bulk-heterojunction solar cells. *Journal of Materials Chemistry* 19 (30): 5416-23.

[92] Li, J., F. Dierschke, J. Wu, A. C. Grimsdale, and K. Müllen. 2006. Poly(2,7-carbazole) and perylene tetracarboxydiimide: A promising donor/acceptor pair for polymer solar cells. *Journal of Materials Chemistry* 16 (1): 96-100.

[93] Rajaram, S., P. B. Armstrong, Bumjoon J. Kim, and J. M. J. Fréchet. 2009. Effect of addition of a diblock copolymer on blend morphology and performance of poly(3-hexylthiophene):Perylene diimide solar cells. *Chemistry of Materials* 21 (9): 1775-7.

[94] Tao, Y., B. McCulloch, S. Kim, and R. A. Segalman. 2009. The relationship between morphology and performance of donor-acceptor rod-coil block copolymer solar cells. *Soft Matter* 5 (21): 4219-30.